Remote Sensing of Environment 140 (2014) 433–449

Contents lists available at ScienceDirect

Remote Sensing of Environment

journal homepage: www.elsevier.com/locate/rse

Conterminous United States demonstration and characterization of MODIS-based Landsat ETM + atmospheric correction

D.P. Roy [a,*], Y. Qin [a], V. Kovalskyy [a], E.F. Vermote [b], J. Ju [c], A. Egorov [a], M.C. Hansen [d], I. Kommareddy [a], L. Yan [a]

[a] Geographic Information Science Center of Excellence, South Dakota State University Brookings, SD 57007, USA
[b] NASA Goddard Space Flight Center, Terrestrial Information Systems Branch, MD 20771, USA
[c] NASA Goddard Space Flight Center and Earth Resources Technology, Inc., Greenbelt, MD 20771, USA
[d] Department of Geographical Sciences, University of Maryland, 2181 Samuel J. LeFrak Hall, College Park, MD 20742, USA

ARTICLE INFO

Article history:
Received 10 November 2012
Received in revised form 9 September 2013
Accepted 10 September 2013
Available online 9 October 2013

Keywords:
Landsat
MODIS
Atmospheric correction
Web-enabled Landsat Data (WELD)

ABSTRACT

The potential of Landsat data processing to provide continental scale 30 m products has been demonstrated by the NASA Web-enabled Landsat Data (WELD) project. The integration of a recent MODIS based Landsat atmospheric correction algorithm into the WELD processing is described and demonstrated by application to 12 months of conterminous United States (CONUS) Landsat 7 ETM + data. A large volume assessment of the atmospheric correction is presented considering approximately 53 million 30 m pixel locations sampled systematically across the CONUS for December 2009 to November 2010. Monthly 30 m reflectance and derived normalized difference vegetation index (NDVI) data are assessed comparing the top of atmosphere (TOA) and the MODIS-based atmospherically corrected surface reflectance values with respect to spectral, temporal, land cover, and a per-pixel atmospheric correction quality storage scheme. The mean CONUS absolute difference between surface and TOA NDVI expressed as a percentage of the surface NDVI was 28% and the surface NDVI was on average 0.1 greater than the TOA NDVI for "vegetated" surfaces. The mean difference between surface and TOA reflectance (surface minus TOA) increased monotonically with increasing surface reflectance. On average the change from a negative to a positive mean difference occurred when the surface reflectance was 0.36, 0.22, 0.17, 0.14, 0.07, and 0.02 for Landsat ETM + reflective bands 1, 2, 3, 4, 5, and 7 respectively. These values are of interest as they depict the average CONUS Landsat ETM + surface reflectance values where the atmosphere has on average no impact and provide the average boundary values for positive and negative atmospheric contributions to ETM + TOA reflectance. The CONUS mean absolute differences between surface and TOA reflectance expressed as percentages of the surface reflectance were 45%, 22%, 12%, 6%, 5%, and 13% for Landsat ETM + bands 1, 2, 3, 4, 5 and 7 respectively.

1. Introduction

The potential of Landsat data processing to provide systematic continental scale products has been demonstrated by the NASA Web-enabled Landsat Data (WELD) project that has generated 30 m composited Landsat weekly, monthly, seasonal and annual mosaics of the conterminous United States (CONUS) and Alaska (Roy et al., 2010; WWW1). The most recent WELD products provide top of atmosphere (TOA) reflectance for each of the six reflective wavelength Landsat 7 Enhanced Thematic Mapper plus (ETM+) bands (WWW2). Surface reflectance, i.e., TOA reflectance corrected for atmospheric effects, is needed to derive consistent geophysical and biophysical products because the impact of atmospheric gases and aerosols on optical wavelength radiation is variable in space and time. Systematic atmospheric correction of Landsat data at continental scale is challenging because of the large Landsat data volume. A number of atmospheric correction methodologies have been developed but those using radiative transfer algorithms and atmospheric characterization data provide the most potential for automated large area application. For example, the MODIS reflective wavelength bands are atmospherically corrected using the 6SV radiative transfer code to generate global daily and 8-day surface reflectance products since 2000 (Justice et al., 2002; Vermote, El Saleous, & Justice, 2002). Recently, the accuracy of two radiative transfer based Landsat atmospheric corrections algorithms, the Landsat Ecosystem Disturbance Adaptive Processing System (LEDAPS) algorithm (Masek et al., 2006) and a MODIS-based Landsat atmospheric correction algorithm (Ju, Roy, Vermote, Masek, & Kovalskyy, 2012), was assessed by a comparison of atmospherically corrected Landsat ETM+ subsets with ETM+ surface reflectance derived independently using the 6SV radiative transfer code parameterized with AERONET sun-photometer retrievals (Ju et al., 2012). The MODIS-based algorithm was more accurate than

* Corresponding author.
E-mail address: david.roy@sdstate.edu (D.P. Roy).

0034-4257
http://dx.doi.org/10.1016/j.rse.2013.09.012

the LEDAPS for all the Landsat ETM+ bands except the green band, where the results for the two methods were comparable, and the blue band where both the LEDAPS and MODIS-based atmospheric correction methods performed less reliably (Ju et al., 2012).

This paper demonstrates the operationalization of the MODIS-based Landsat atmospheric correction algorithm integrated into the WELD processing chain. It is well established that although validation exercises, such as reported by Ju et al. (2012), provide product accuracy information, only examination of a large spatial and temporal product sample will enable characterization of product performance (Roy et al., 2002). A comprehensive product characterization comparing more than 50 million 30 m pixels extracted from one year of monthly CONUS 30 m TOA and surface reflectance WELD processed Landsat ETM+ data is presented to provide a quantitative assessment of the impact of the atmospheric correction on the Landsat 7 ETM+ bands. The impact on the derived normalized difference vegetation index (NDVI) is also considered as it is one of the most commonly used remote sensing indices.

The WELD Landsat 7 ETM+ data processing used to generate monthly CONUS TOA reflectance products is first described and then the MODIS-based atmospheric correction implementation, including an atmospheric correction product per-pixel quality storage scheme, is described. The analysis methodology is described considering spectral, temporal, land cover and quality aspects of differences imposed by the atmospheric correction. The results are followed by concluding remarks including the implications for atmospheric correction of global Landsat data using this approach.

2. Data and pre-processing

2.1. Landsat ETM + input data

Landsat 7 ETM+ data were obtained from the U.S. Geological Survey Earth Resources Observation and Science (EROS) Center Landsat archive. Landsat data are nominally processed to a Level 1 terrain corrected (L1T) level defined in GeoTIFF format in the Universal Transverse Mercator (UTM) map projection. All the Landsat ETM+ L1T data over the CONUS with cloud cover ≤80% were obtained for the period December 2009 to November 2010, a total of 8116 Landsat L1T scenes. As the purpose of this study is to demonstrate and characterize the CONUS wide atmospheric correction, a high 80% cloud cover threshold was used; this is also the cloud cover threshold used to select the L1T data used to generate the CONUS WELD products (available at WWW2). The month of February 2010 had the fewest scenes (479) and August 2010 the greatest number of scenes (884) which is due to seasonal CONUS cloud variability at the time of Landsat overpass (Ju & Roy, 2008). Each Landsat L1T scene is approximately 180 km by 170 km and because of the ETM+ scan line corrector (SLC) failure has 22% missing pixels occurring in a repeating along-scan stripe pattern (Markham, Storey, Williams, & Irons, 2004).

Only L1T data were used to reduce the impact of misregistration errors, particularly on the WELD temporally composited products (Roy, 2000; Roy et al., 2010). The CONUS L1T geolocation error is <30 m even in areas with substantial terrain relief (Lee, Storey, Choate, & Hayes, 2004). The reflective band calibration uncertainty for Landsat 7 ETM+ is 5% (Markham & Helder, 2012). All six 30 m reflective Landsat ETM+ wavelength bands were used: blue (band 1: 0.45–0.52 μm), green (band 2: 0.53–0.61 μm), red (band 3: 0.63–0.69 μm), near-infrared (band 4: 0.78–0.90 μm), and two middle-infrared (bands 5 and 7: 1.55–1.75 μm and 2.09–2.35 μm).

2.2. WELD Landsat pre-processing, projection, and compositing into monthly tile products prior to atmospheric correction

The Landsat ETM+ L1T data were processed using the Version 1.5 WELD processing algorithms (Roy et al., 2010, 2011). This processing first converts the digital numbers in each L1T acquisition to top of atmosphere (TOA) reflectance and derived pixel values, then projects the data into a continental projection in fixed Earth-located tiles, and then applies a per-pixel temporal compositing algorithm to select the best Landsat observation within the product compositing period (weekly, monthly, seasonal, annual). For this study 12 monthly composites defined for each month from December 2009 to November 2010 were generated.

For each Landsat L1T acquisition the TOA reflectance for the six reflective ETM+ bands, the TOA brightness temperature for the two thermal bands, bit packed band saturation information, the TOA Normalized Difference Vegetation Index (NDVI), defined as the near-infrared minus the red reflectance divided by their sum (Tucker, 1979), and two cloud masks were generated. The cloud masks were the heritage Landsat project automatic cloud cover assessment algorithm (ACCA) (Irish, Barker, Goward, & Arvidson, 2006) and a decision tree cloud mask algorithm that generally performs better than ACCA for Landsat ETM+ over the CONUS (Roy et al., 2010). The data were projected from UTM coordinates to the Albers Equal Area projection defined with standard parallels and central meridians used by the USGS EROS National Land Cover Database product (Homer, Huang, Yang, Wylie, & Coan, 2004). The Landsat pixels were allocated to the Albers coordinate system using the inverse gridding approach that is geometrically equivalent to nearest neighbor resampling (Wolfe, Roy, & Vermote, 1998). The projected data were defined in the standard 501 WELD CONUS tiles of 5000 × 5000 30 m Landsat pixels (Roy et al., 2011).

Compositing procedures were applied independently on a per-pixel basis to the gridded Albers WELD processed data sensed over the same area in each month (Roy et al., 2010). The Version 1.5 WELD compositing algorithm incorporates the heritage maximum NDVI and maximum brightness temperature compositing criteria as clouds and aerosols typically depress NDVI and brightness temperature over land (Cihlar, Manak, & D' Iorio, 1994; Holben, 1986; Roy, 1997). Importantly, the WELD compositing was applied before atmospheric correction because (i) the atmospheric correction is imperfect (Ju et al., 2012) and (ii) because in this way only the composited gridded WELD pixel values need to be atmospherically corrected rather than every pixel in every input Landsat L1T acquisition. In the composited monthly tiled products the day of year that each 30 m pixel was sensed on and the number of Landsat observations considered in the month were stored (Roy et al., 2011). To support the subsequent atmospheric correction, an index value (0, 1, … 255) to the input L1T filename that each composited pixel was selected from was stored (illustrated bottom left, Figs. 1 and 2). The index values were stored with the corresponding L1T filename and L1T acquisition scene center solar view and azimuth angle in the tile product metadata.

3. MODIS-based Landsat atmospheric correction

3.1. Atmospheric correction overview and validation summary

The MODIS-based atmospheric correction methodology and validation is described in detail in Ju et al. (2012). The Landsat 7 ETM+ TOA reflectance are atmospherically corrected using the 6SV radiative transfer code (Kotchenova et al., 2006) with contemporaneous MODIS Terra derived atmospheric characterization data. The algorithm works because both sensors are in the same polar orbit, with Landsat ETM+ observations occurring approximately 25 minutes before MODIS Terra nadir observations. The MODIS Terra derived atmospheric characterization data are defined over the CONUS for each day in 0.05° × 0.05° grid cells. The aerosol optical thickness at 550 nm, and the aerosol type (low absorption smoke, high absorption smoke, polluted urban, and clean urban types) are derived dynamically from the MODIS shortwave visible ocean and land bands using an improved non-linear version of the Kaufman et al. (1997) dense dark vegetation methodology (Vermote & Kotchenova, 2008). The water vapor is derived directly from the

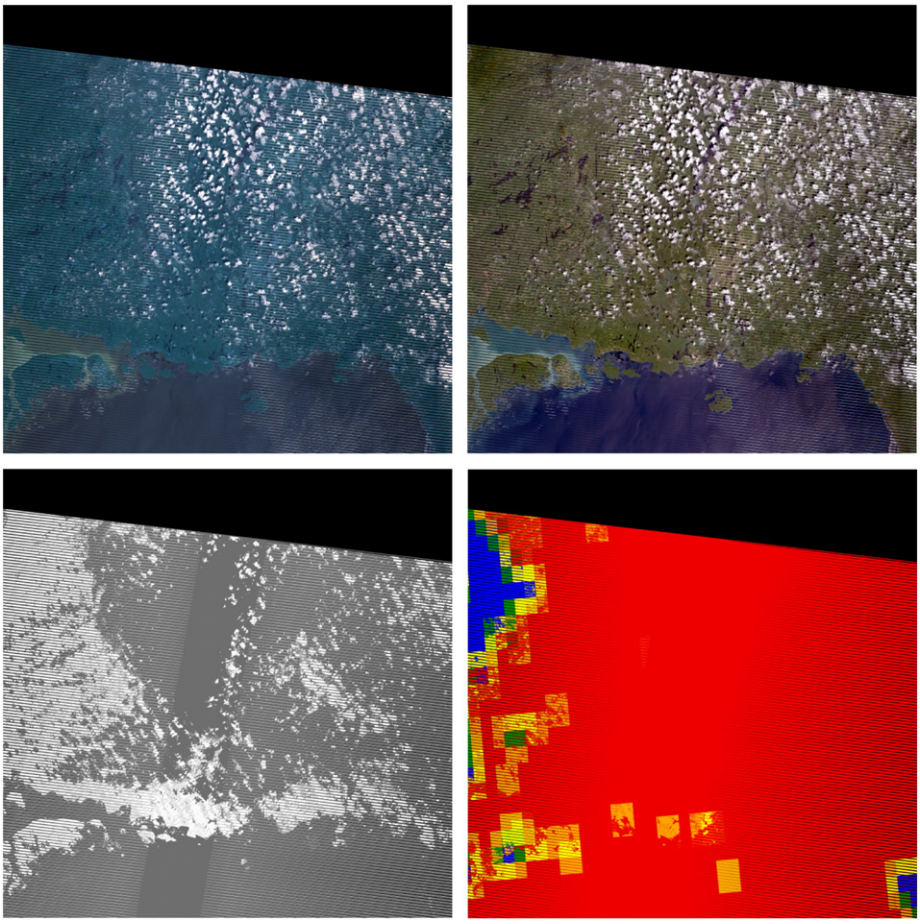

Fig. 1. Illustration of MODIS-based Landsat atmospheric correction for a 5000 × 5000 30 m pixel tile, north shore of Lake Superior (WELD tile h21v02), July 2010 monthly composite generated from two Landsat ETM + acquisitions sensed 16 days apart on July 9th and 25th 2010 with scene center solar zenith angles of 31.23° and 33.82° respectively. Top left: Top of atmosphere (TOA) true color red (0.63–0.69 μm), green (0.53–0.61 μm) and blue (0.45–0.52 μm), reflectance; top right: MODIS-based atmospherically corrected equivalent, shown with exactly the same red, green and blue display stretch parameters as the illustrated TOA data; bottom left: Input L1T filename index, white = July 9th 2010 and gray = July 25th 2010; bottom right: atmospheric correction quality indicator — the number of natural neighbor interpolated MODIS 0.05° atmospheric correction coefficients (blue = 0, green = 1, orange = 2, yellow = 3, red = 4).

MODIS near-infrared water vapor bands (typical accuracy 5–10%) (Vermote & Kotchenova, 2008), atmospheric pressure at sea level is defined by NCEP/NCAR 6-hourly Reanalysis data, and NCEP ozone is derived from NASA NOAA Total Operational Vertical Sounder (TOVS) ozone retrievals (typical accuracy 0.02 cm·atm). Sea level atmospheric pressure is adjusted to surface level using a one arc-second resolution ASTER digital elevation model by multiplying the sea level pressure with the negative exponent of the quotient of the digital elevation and an 8000 m scale height (Vermote & Saleous, 2006).

The MODIS-based Landsat atmospheric correction algorithm was validated by a comparison of 10 km × 10 km 30 m atmospherically corrected Landsat ETM + subsets with surface reflectance derived independently using the 6SV radiative transfer code parameterized with AERONET sun-photometer retrievals (Dubovik et al., 2002; Holben et al., 1998). A total of 95 subsets located across the CONUS and sensed at different times of the year under different atmospheric conditions were used for the validation (Ju et al., 2012). The mean absolute residuals between AERONET corrected surface reflectance and the MODIS-based atmospherically corrected reflectance, expressed as percentages of the mean AERONET surface reflectance, were 13.5%, 5.7%, 4.2%, 2.0%, 1.0% and 1.6% for the Landsat ETM + blue (0.45–0.52 μm), green (0.53–0.61 μm), red (0.63–0.69 μm), near-infrared (0.78–0.90 μm), and the two middle-infrared bands (1.55–1.75 μm and 2.09–2.35 μm) respectively (Ju et al., 2012).

3.2. Atmospheric correction implementation integrated into the WELD processing

All the pixels selected by the compositing process from the same Landsat 7 ETM + L1T acquisition were atmospherically corrected in each 5000 × 5000 pixel WELD tile using the procedure described below. The procedure was repeated for the different sets of pixels selected from different L1T acquisitions until all the pixels in the tile were corrected.

3.2.1. Landsat spectral band atmospheric correction coefficient computation

The MODIS derived 0.05° × 0.05° atmospheric characterization data for the day that the Landsat L1T data were sensed on were used to generate CONUS 0.05° × 0.05° maps of atmospheric correction coefficients. The following four atmospheric correction coefficients were defined for each Landsat ETM + reflective wavelength band: ρ_{atm}, T_d, T_u, and s_{atm}, where ρ_{atm} is the atmospheric intrinsic reflectance, T_d is the downward atmospheric transmission in the direction of light propagation from the TOA to the surface, T_u is the upward atmospheric transmission in the direction of light propagation from the surface to the sensor, and s_{atm} is the atmospheric spherical albedo (Ju et al., 2012). The coefficients were generated using pre-computed 6SV look up tables populated by forward modeling the 6SV code. The look up tables were parameterized by ETM + spectral band number, aerosol optical thickness, surface

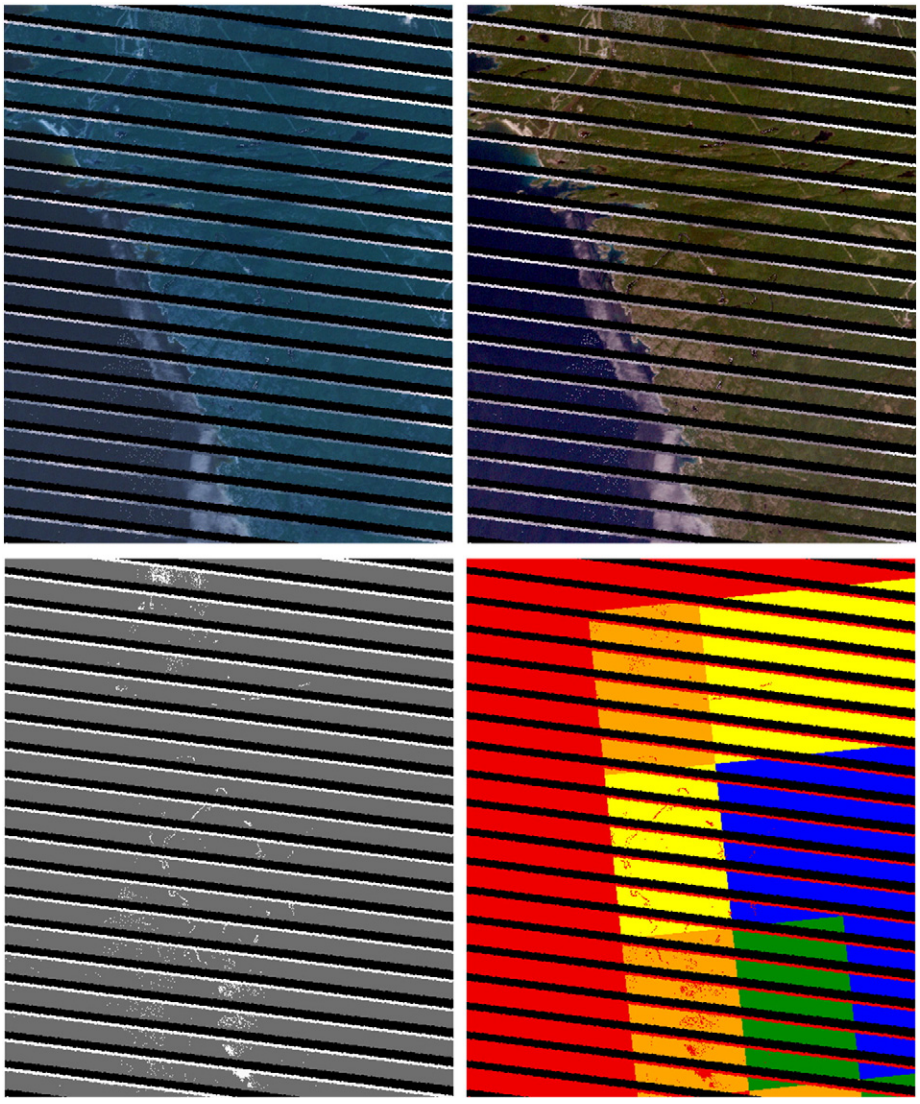

Fig. 2. Detail of Fig. 1, illustrating 500 × 600 30 m pixel subsets extracted from the south west corner of Fig. 1. The Landsat ETM+ scan line corrector gaps are clearly evident. Only two temporally overlapping Landsat ETM+ acquisitions sensed 16 days apart were composited in this WELD tile and the majority of the pixels were selected from the July 25th 2010 (gray, bottom left) rather than the July 9th 2010 acquisition (white, bottom left). In this subset the July 9th 2010 acquisition was primarily cloudy (white stripes, top row) and many of the MODIS 0.05° atmospheric correction coefficients were interpolated (blue = 0, green = 1, orange = 2, yellow = 3, red = 4; bottom right).

atmospheric pressure, and the solar and view geometry. The solar zenith and azimuth for the Landsat L1T scene center were used with a 3.5° view zenith angle (i.e. half way from nadir to the ETM+ swath edge) as for the LEDAPS code (Masek et al., 2006). Ozone, water vapor other gas absorptions were calculated using empirical fits based on 6SV forward modeling.

The four 0.05° × 0.05° atmospheric correction coefficients were generated for each Landsat L1T acquisition day and solar geometry for all the CONUS. Typically about 50% of the CONUS 0.05° × 0.05° grid cells have no atmospheric characterization data and hence no atmospheric correction coefficients. This is due to clouds at the time of MODIS Terra overpass and so the amount of missing data varies with location and season. To resolve this issue the gaps in each of the CONUS 0.05° × 0.05° atmospheric correction coefficients were filled by natural neighbor interpolation. The natural neighbor interpolation approach can handle irregular and sparse data, requires no tuning parameters, and the interpolated values are guaranteed to be within the range of the samples used (Sibson, 1981). The natural neighbor interpolation was performed independently for each of the four atmospheric correction coefficients across all the CONUS 0.05° × 0.05° grid cells to preserve the original atmospheric correction coefficient values where they were defined and to interpolate any missing 0.05° grid cell values (Ju et al., 2012).

3.2.2. Surface reflectance computation

The location of each 30 m tile pixel was projected into the 0.05° × 0.05° CONUS atmospheric correction coefficient data derived for that pixel's Landsat L1T acquisition day and solar geometry. The atmospheric correction coefficient values at the projected 30 m pixel location were derived by bilinear interpolation of the four neighboring 0.05° × 0.05° grid cell values (Ju et al., 2012). The surface reflectance for each Landsat ETM+ reflective wavelength band was then computed as:

$$\rho^s = \frac{\left(\rho^{TOA}/c_1 - c_2\right)/c_3}{((\rho^{TOA}/c_1 - c_2)/c_3)c_4 + 1} \quad (1)$$

where ρ^s and ρ^{TOA} are the surface and TOA reflectance respectively (nominal range 0–1), and $c_1 = T_d$, $c_2 = \rho_{atm}/T_d$, $c_3 = T_u$, and $c_4 = s_{atm}$ are the atmospheric correction coefficients (Ju et al., 2012). The surface

Normalized Difference Vegetation Index ($NDVI^s$) was derived as the near-infrared minus the red surface reflectance divided by their sum.

3.2.3. Atmospheric correction quality indicator computation

The Landsat atmospheric correction is expected to be less accurate at locations where there were missing MODIS atmospheric characterization data, i.e., at locations where natural neighbor interpolated MODIS atmospheric characterization values were used. Consequently, as in Ju et al. (2012), a count of how many (0–4) of the four 0.05° atmospheric correction coefficient pixels that were natural neighbor interpolated was stored for each 30 m pixel to provide an atmospheric correction quality indicator.

3.3. Atmospheric correction implementation illustrative results

Fig. 1 illustrates example TOA Landsat 7 ETM+ visible wavelength reflectance and corresponding MODIS-corrected Landsat surface reflectance for a single monthly 5000 × 5000 30 m WELD tile (top row). This particular example was selected as it includes only two Landsat ETM+ L1T acquisitions sensed 16 days apart (on July 9th and July 25th) and so the results are simpler to interpret than for other tile examples where more and laterally overlapping L1T acquisitions were processed. In addition, this example is representative of typical conditions where the Landsat L1T acquisitions and the CONUS MODIS 0.05° × 0.05° atmospheric characterization data are cloud contaminated at different locations (Ju & Roy, 2008; Roy, Lewis, Schaaf, Devadiga, & Boschetti, 2006). Moreover, these data show spatial variability in the compositing selection of different Landsat L1T acquisitions and in the atmospheric correction quality indicator (bottom row).

The impact of the atmospheric correction on the TOA reflectance is obvious visually (Fig. 1, top row). Adjacent 30 m pixels may be selected by the compositing algorithm from different Landsat acquisitions. This is evident in the bottom left of Fig. 1 that shows the input L1T filename index and illustrates that across the tile the composited pixels were selected from the two L1T acquisitions in a variable way. This variation is dependent upon the degree of cloudiness of the two Landsat acquisitions and on the efficacy of the compositing algorithm. The bottom right of Fig. 1 shows the atmospheric correction quality indicator i.e., a count of how many of the four 0.05° atmospheric correction coefficient pixels used to atmospherically correct each 30 m pixel were natural neighbor interpolated. For this example most 30 m pixels had four 0.05° interpolated values (red) and their atmospheric correction is expected to be less reliable than the pixels with fewer interpolated values. Only a minority of pixels had no interpolated atmospheric correction coefficients (blue) and these tend to be away from cloudy locations as clouds preclude the MODIS Terra atmospheric characterization data retrievals.

Fig. 2 illustrates a 500 × 600 30 m pixel subset of Fig. 1. The Landsat ETM+ scan line corrector (SLC) gaps are clearly evident at this scale. A fill value is defined (black in Figs. 1 and 2) where there were no L1T data sensed over the month. The majority of the pixels in the subset were selected by the compositing algorithm from the July 25th acquisition (gray, bottom left) rather than from the July 9th acquisition (white, bottom left). Where there were clouds in both acquisitions or in the only sensed acquisition a cloudy pixel was selected by the compositing algorithm (evident by the white stripes in the TOA and surface reflectance, top row). The majority of the 30 m pixels used several interpolated MODIS 0.05° atmospheric correction coefficients (non-blue colors, bottom right) and are related to clouds (most obviously for the pixels selected from the July 9th acquisition). As adjacent 30 m pixels may be selected from different L1T acquisitions their atmospheric correction quality indicator values may be quite different (evident by the red stripes along the bottom of each SLC-off gap, bottom right).

4. Analysis methodology

The MODIS-based atmospheric correction methodology was applied independently to each 5000 × 5000 30 m pixel CONUS tile and for each of the 12 monthly periods. The resulting TOA and surface reflectance data were compared following the MODIS land product quality assessment approach (Roy et al. 2002) by first undertaking a qualitative synoptic visual assessment and then a quantitative examination of a large data sample. Spectral, temporal, land cover, and quality, aspects of differences imposed by the atmospheric correction were examined.

4.1. Qualitative analysis

Qualitative visual comparison of the TOA and MODIS-corrected Landsat surface reflectance was first undertaken by examination of CONUS true color (red, green, blue reflectance) images. Because the CONUS covers approximately 11,000,000,000 30 m land pixels only CONUS images with a reduced spatial resolution could be displayed. Browse CONUS images with a spatial resolution of approximately 150 m were generated by selecting within spatially adjacent non-overlapping 5 × 5 30 m pixel windows the pixel with the median red reflectance and the corresponding blue and green reflectance values for that pixel. In this way, the reflectance for the same pixel was obtained which produced a more coherent true color reflectance browse than selecting the median reflectance values for each visible band wavelength independently (Roy et al., 2010). The red reflectance was used as the "master" in the selection process since it is less sensitive to atmospheric contamination than the shorter wavelength blue and green reflectance bands (Ju et al., 2012; Ouaidrari & Vermote, 1999). CONUS browse images were generated independently using the TOA and MODIS-corrected surface reflectance.

4.2. Quantitative analysis

4.2.1. Data sampling

Pixels were sampled every 40 rows and 40 columns across each CONUS monthly composited tile, and only the non-missing pixel values extracted (for example, missing pixels are shown as black in Figs. 1 and 2). The reflectance derived from saturated radiance is unreliable and so the saturated spectral values were discarded. Landsat 7 ETM+ saturation can occur in any of the reflective bands, typically when pixels contain illuminated thick cumulonimbus cloud, illuminated snow, or sunglint over water (Bindschadler et al., 2008; Cahalan et al., 2001; Dowdeswell & Mcintyre, 1986). Cloudy pixels were discarded using a conservative cloud screening by considering cloudy pixels as those labeled as cloudy in either the ACCA or the decision tree cloud masks. We note that neither cloud mask is perfect and cloudy pixels and sub-pixel clouds may remain (Roy et al., 2010) and even with cloudy pixel removal, aerosol properties near clouds can be different than far from clouds (Tackett & Di Girolamo, 2009), and together may result in residual atmospheric correction errors (Kaufman, 1987; Ouaidrari & Vermote, 1999).

4.2.2. Sample out of range analysis

The percentage of sample data with surface reflectance ($\rho^s{}_\lambda$) and surface NDVI ($NDVI^s$) falling out of nominal theoretical limits was quantified. Atmospherically corrected pixels may have values outside their theoretical limits, i.e. $\rho^s{}_\lambda > 1$ or $\rho^s{}_\lambda < 0$ and $NDVI^s > 1$ or $NDVI^s < -1$, due to "over correction" by the atmospheric correction algorithm, Landsat calibration errors, and due to instrument artifacts not accommodated for by the Landsat calibration (Ju et al., 2012; Markham & Helder, 2012; Roy et al., 2010). In addition, $\rho^s{}_\lambda$ may be greater than 1 for a surface that reflects in the satellite observation direction more strongly than a Lambertian surface (Schaepman-Strub, Schaepman, Painter, Dangel, & Martonchik, 2006).

4.2.3. Sample scatterplot analysis

Scatter plots of the MODIS-based atmospherically corrected surface versus TOA reflectance, and similarly for the derived surface and TOA NDVI, were generated considering all 12 months of sample data. The overall relationship between the surface and TOA values was characterized statistically for each reflective band and for the NDVI using reduced major axis (RMA) linear regression. The RMA rather than conventional ordinary least squares regression was used as it allows for both the dependent and independent variables to have error (Cohen, Maiersperger, Gower, & Turner, 2003) which is required as Landsat atmospheric correction errors are non-negligible (Ju et al., 2012) and the TOA reflectance contains 5% calibration errors (Markham & Helder, 2012).

Multiple scattering of reflected radiation between the surface and the atmosphere introduces a dependency between the surface reflectance and the atmospheric contribution to the TOA reflectance (Kaufman & Sendra, 1988; Tanre, Herman, & Deschamps, 1981). To explore the dependence of the atmospheric correction with surface reflectance, summary statistics of the difference between the surface and TOA reflectance were derived over contiguous surface reflectance ranges. At any given 30 m pixel the difference between the MODIS-based atmospherically corrected surface and TOA reflectance may be defined as:

$$\Delta\rho_{i,\lambda} = \rho^{s}{}_{i,\lambda} - \rho^{TOA}{}_{i,\lambda} \tag{2}$$

where $\rho^{s}{}_{i,\lambda}$ and $\rho^{TOA}{}_{i,\lambda}$ are the MODIS-based atmospherically corrected surface and TOA reflectance respectively and $\Delta\rho_{i,\lambda}$ is their difference for Landsat reflective band λ for some sampled pixel *i*. To explore the dependence of the atmospheric correction with surface reflectance, the mean and standard deviation of the difference between the surface and TOA reflectance, were derived over 100 contiguous surface reflectance ranges from 0 to 1 as:

$$\overline{\Delta}\rho_{\lambda,k} = \left(\sum_{i=1}^{n_{\lambda,k}} \Delta\rho_{i,\lambda}\right) \Big/ n_{\lambda,k} \tag{3}$$

$$\sigma_{\Delta\rho_{\lambda,k}} = \left(\sum_{i=1}^{n_{\lambda,k}} \left(\Delta\rho_{i,\lambda} - \overline{\Delta}\rho_{\lambda,k}\right) \Big/ n_{\lambda,k} - 1\right)^{\frac{1}{2}} \tag{4}$$

for $k = 1, 2, 3 \ldots 100$ where each k describes the set of pixels where $\frac{k-1}{100} \le \rho^{s}{}_{i,\lambda} < \frac{k}{100}$ and where $\overline{\Delta}\rho_{\lambda,k}$ and $\sigma_{\Delta\rho_{\lambda,k}}$ are the mean and standard deviation of the difference between the surface and TOA reflectance respectively considering $n_{\lambda,k}$ sampled pixel locations for Landsat band λ. The number of 30 m pixels $n_{\lambda,k}$ typically varies with Landsat band λ because the degree of Landsat saturation varies among bands. The measures $\overline{\Delta}\rho_{\lambda,k}$ and $\sigma_{\Delta\rho_{\lambda,k}}$ were computed using all 12 months of sample data and plotted against the $k = 1, 2, 3 \ldots 100$ contiguous surface reflectance ranges.

4.2.4. Sample TOA to surface mean and relative absolute difference analysis

The mean absolute difference between the surface and TOA was derived to quantify the average magnitude of the atmospheric correction for each reflective wavelength band as:

$$|\overline{\Delta}|\rho_{\lambda} = \left(\sum_{i=1}^{n_{\lambda}} |\Delta\rho_{i,\lambda}|\right) / n_{\lambda} \tag{5}$$

where $|\overline{\Delta}|\rho_{\lambda}$ is the mean absolute difference between the surface and TOA reflectance considering n_{λ} sampled 30 m pixel locations for Landsat band λ, and $\Delta\rho_{i,\lambda}$ is defined as Eq. (2).

In addition, in order to be able to inter-compare $|\overline{\Delta}|\rho_{\lambda}$ between spectral bands, that can have very different reflectance magnitudes for the same scene components, for example, healthy vegetation has low red reflectance and high near-infrared reflectance, the mean reflectance normalized absolute percentage difference was derived as:

$$|\overline{\Delta}|^{*}\rho_{\lambda} = \left(\frac{|\overline{\Delta}|\rho_{\lambda}}{\sum_{i=1}^{n_{\lambda}} \rho^{s}_{i,\lambda} \Big/ n_{\lambda}}\right) 100 \tag{6}$$

where $|\overline{\Delta}|\rho_{\lambda}$ is the mean absolute difference between the surface and TOA reflectance (Eq. (5)), considering n_{λ} sampled 30 m pixel locations for Landsat band λ and $\rho^{S}{}_{i,\lambda}$ is the MODIS-based atmospherically corrected surface reflectance respectively for sampled pixel *i*. The measures $|\overline{\Delta}|\rho_{\lambda}$ and $|\overline{\Delta}|^{*}\rho_{\lambda}$ were computed using all 12 months of sample data. Similarly, the differences between the surface NDVI and TOA NDVI were also quantified as above.

4.2.5. Sample atmospheric correction quality analysis

The quantitative analyses were repeated using only "good" quality 30 m atmospherically corrected pixels defined as those pixels computed using no natural neighbor interpolated MODIS 0.05° atmospheric correction coefficients. In this way the impact of the quality of the MODIS-based Landsat atmospheric correction captured by the 0.05° MODIS atmospheric correction coefficient interpolation count (Figs. 1 and 2, bottom right) was examined.

4.3. Temporal land cover based analysis

As surface and atmospheric conditions change seasonally a temporal analysis was undertaken to compare the monthly TOA and MODIS-corrected surface reflectance and derived NDVI. Time series of LEDAPS atmospherically corrected WELD 30 m NDVI have shown good correspondence with flux tower derived NDVI (Kovalskyy, Roy, Zhang, & Ju, 2011). In this study however rather than examine a small number of 30 m data over flux towers, a large number of CONUS pixels were examined over bare ground and forest classified pixels. A CONUS Land Cover Land Cover Change (LCLCC) product that includes a 30 m classification of maximum Tree Crown cover (0–100%) and minimum Bare Ground (0–100%) cover was used to define these two classes. Pixels with <50% bare ground and >50% tree crown cover were considered as forest, and pixels with >50% bare ground and <50% tree crown cover were considered as bare ground. In this way a total of 852,608,105 bare ground and 2,329,985,614 forest CONUS 30 m pixels were defined and are illustrated in Fig. 3. The CONUS LCLCC product was generated from 5 years (2006 to 2010) of WELD products (Hansen et al., 2013) using high spatial resolution training data and supervised regression tree classification approaches based on the approaches described in Hansen, Stehman, and Potapov (2010) and Hansen et al. (2011), and is available at WWW3.

Pixels were sampled every 20 rows and 20 columns across each CONUS monthly composited tile, and if the pixel was forest or bare ground the value was extracted. Cloudy and saturated pixel values were discarded as described in Section 4.2.1. The forest pixels include deciduous and coniferous tree species and the bare ground pixels include both bare soil and impermeable urban areas. This broad spatial definition and any classification errors will introduce within-class variability. Consequently, both the mean and standard deviation of the TOA and surface reflectance and derived NDVI were computed for each of the 12 monthly products for these two classes.

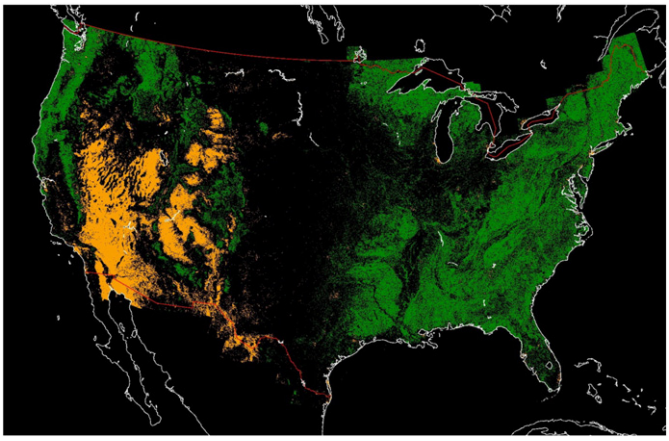

Fig. 3. CONUS Forest (green) and Bare Ground (orange) locations derived from the 30 m 5-year (2006 to 2010) WELD Land Cover Land Cover Change (LCLCC) product (Hansen et al., 2013). In this illustration each pixel is generalized from 5 × 5 30 m Landsat pixels to provide an approximate spatial resolution of 150 m. The forest 150 m pixels are those where the majority of the 25 30 m LCLCC pixels falling within contiguous 5 × 5 30 m pixel subgrids are labeled as >50% forest and <50% bare ground, similarly the bare ground 150 m pixels are labeled as those where the majority of the 25 30 m LCLCC pixels are labeled as >50% bare ground and <50% forest. The red vector shows the northern and the southern border of the CONUS. All the WELD tiles including those illustrated falling north and south of the border are considered; a total of 852,608,105 30 m Bare Ground pixels and 2,329,985,614 Forest 30 m pixels.

5. Results

5.1. Qualitative results

Figs. 4 and 5 show the July monthly TOA and MODIS-corrected surface visible reflectance browse images respectively that were generated by WELD processing 851 Landsat ETM+ scenes. The same "honest" contrast stretch was used for both figures, showing the three visible bands with the same red, green and blue display stretch parameters. The large black gaps in the two figures are where there were no L1T data with cloud cover ≤80% and so were not processed. Qualitatively the TOA reflectance (Fig. 4) and surface reflectance (Fig. 5) appear quite different with less visual contrast in the TOA reflectance and a more blue appearance due to the impact of the atmosphere at the visible wavelengths. This is also seen at higher resolution for the single tile results illustrated in the top rows of Figs. 1 and 2. The July 2010 browse is illustrated as July is the middle of the summer and nominally captures CONUS peak vegetation conditions.

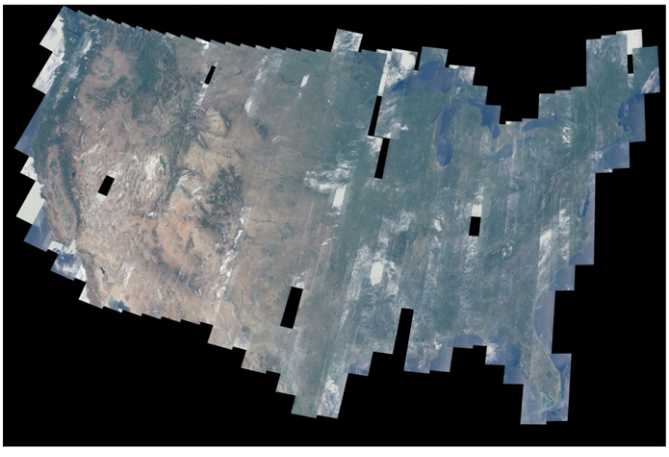

Fig. 4. Top of atmosphere true color reflectance, red (0.63–0.69 μm), green (0.53-0.61 μm) and blue (0.45–0.52 μm), CONUS WELD monthly composite, July 2010. Product composed of 851 Landsat ETM+ scenes with cloud cover ≤80%, Albers Projection. An "honest" contrast stretch is used, showing the three visible bands with exactly the same red, green and blue display stretch parameters. A browse image is displayed where each pixel is generalized from 5 × 5 30 m Landsat pixels to provide an approximate spatial resolution of 150 m.

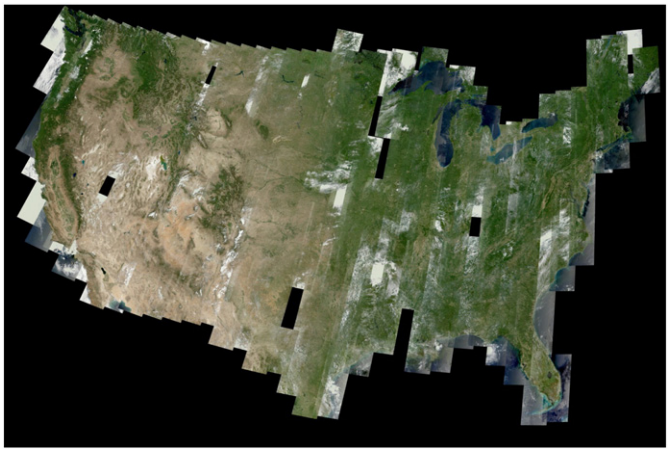

Fig. 5. MODIS based atmospheric correction of the CONUS WELD July 2010 true color reflectance shown in Fig. 4 and illustrated and with the same "honest" contrast stretch.

Fig. 6 shows histograms of the CONUS July red, green, blue, and near-infrared TOA and MODIS-corrected surface reflectance. The histograms were computed from about 5.5 million 30 m pixels sampled every 40 rows and 40 columns across the CONUS. The surface blue, green and red reflectance histogram peak values are 0.07, 0.03 and 0.015 smaller than the TOA blue, green and red reflectance peaks respectively. This is expected due to the greater atmospheric effects at shorter wavelengths associated primarily with aerosol scattering (Kaufman, 1989). After atmospheric correction the red and blue reflectance histogram peaks become more similar to each other and the green reflectance histogram peak is greater than either which is expected given that in July the CONUS is dominated by green vegetation. The NIR histogram is more complex than the visible wavelength histograms and has a bimodal shape. The near-zero NIR reflectance histogram peak is associated with water bodies (lakes, rivers, coastal waters) and the surface NIR peak is about 0.01 smaller than the TOA NIR peak. The histogram NIR reflectance values characteristic of soil surfaces (NIR reflectance approximately 0.1 to 0.3) occur less frequently for the surface than the TOA NIR reflectance. Conversely, the histogram NIR reflectance values characteristic of vegetated surfaces (NIR reflectance greater than approximately 0.35) occur more frequently for the surface than the TOA NIR reflectance. The impact of the atmospheric correction on the TOA NIR reflectance is due primarily to correction for water vapor absorption (Kaufman, 1989). For all four spectral bands illustrated in Fig. 6 there are some atmospherically corrected pixels with negative reflectance, predominantly over water; this effect also occurs in the MODIS surface reflectance product (Vermote et al., 2002) and is quantified in Section 5.2.1.

Fig. 7 shows histograms of the NDVI derived from the July TOA and MODIS-corrected 30 m surface reflectance. The surface NDVI has a greater dynamic range than the TOA NDVI and the NDVI histogram peak is nearly 0.1 higher (peak at 0.88) than the TOA NDVI (peak at 0.77) which has been observed and modeled by other researchers (Holben, 1986; McDonald, Gemmell, & Lewis, 1998). Atmospheric effects generally reduce NDVI but are complex and vary as a function of factors including the degree of aerosol and water vapor contamination and the vegetation cover and soil brightness (Holben, 1986; Huete, 1988; Kaufman & Tanre, 1992; Liu & Huete, 1995; McDonald et al., 1998; Miura, Huete, Yoshioka, & Holben, 2001). For surfaces with low red and near-infrared reflectance the NDVI is particularly sensitive to

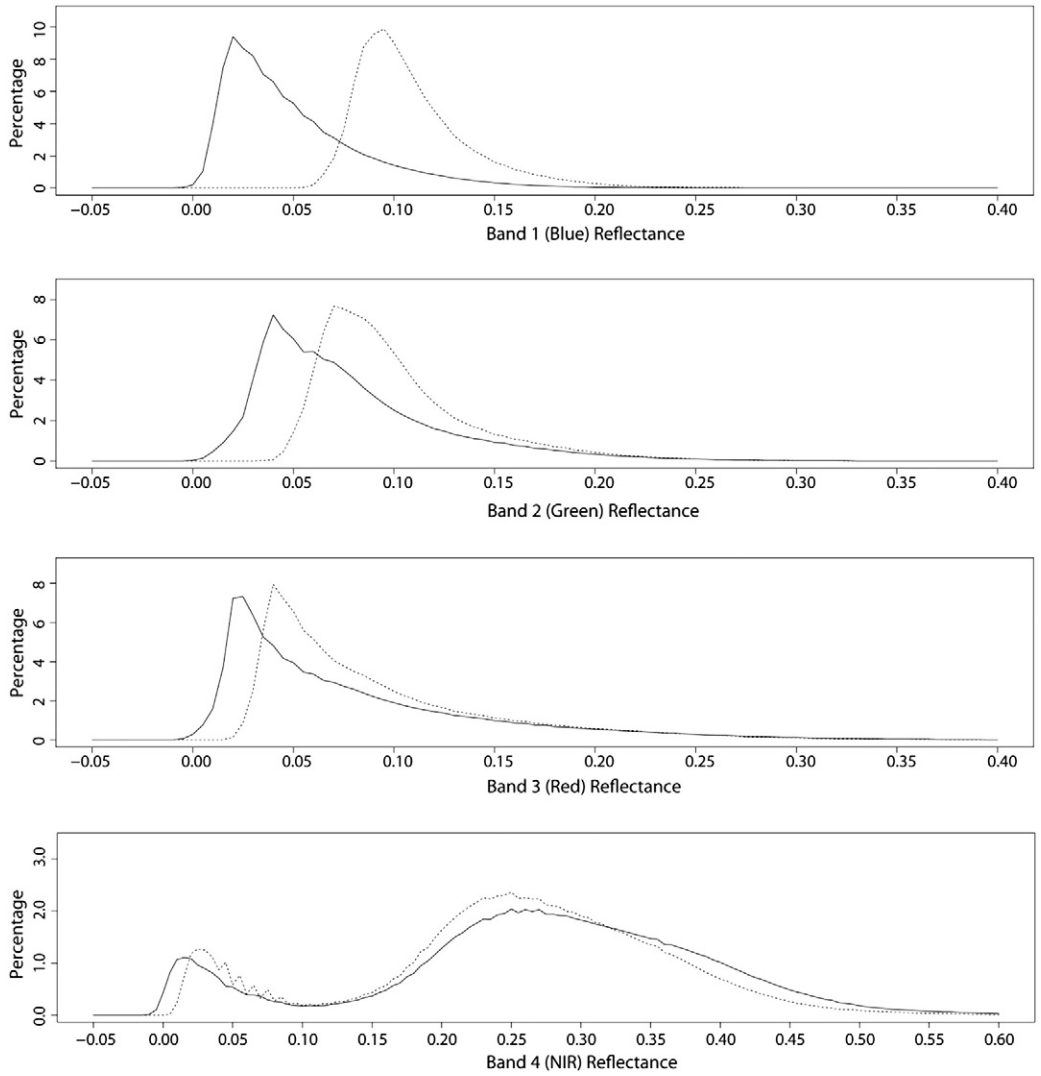

Fig. 6. Histograms of the top of atmosphere (dashed line) and the MODIS-corrected surface (solid line) blue (0.45–0.52 μm), green (0.53–0.61 μm), red (0.63–0.69 μm), and near-infrared (0.78–0.90 μm) Landsat reflectance extracted from the CONUS WELD July 2010 monthly products illustrated in Figs. 4 and 5 respectively. Data extracted by sampling regularly every 40 rows and 40 columns and discarding all cloudy and saturated 30 m WELD pixels. A total of 5,495,934 (blue), 5,496,248 (green), 5,495,835 (red), and 5,494,317 (near-infrared) 30 m pixels considered. Histogram X-axis bin widths of 0.005 reflectance.

atmospheric correction and calibration errors because of the NDVI ratio formulation (Verstraete & Pinty, 1996). The histogram NDVI values characteristic of "non-vegetated" surfaces, i.e., within approximately −0.1 to 0.1, occur more frequently for the surface NDVI than the TOA NDVI. This is associated with low red and near-infrared reflectance over water bodies. Over many CONUS water bodies the atmospheric correction reduced both the red and near-infrared TOA reflectance (Fig. 6) but with greater reductions in the red rather than the near-infrared and consequently the surface NDVI was increased relative to the TOA NDVI.

The differences illustrated in Figs. 6 and 7 reflect surface and atmospheric variations across the CONUS and the efficacy of the MODIS-based atmospheric correction. However, histogram based analyses do not provide insights on the impact of the atmosphere on specific pixel values or land cover conditions and this is investigated quantitatively in Sections 5.2 and 5.3 respectively.

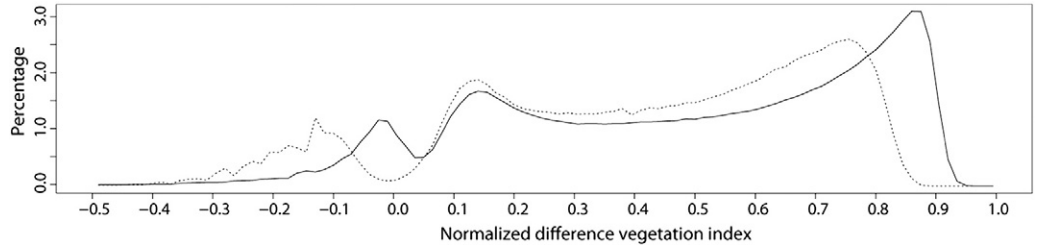

Fig. 7. Histograms of the NDVI derived from the top of atmosphere (dashed line) and the MODIS-corrected surface (solid line) reflectance extracted from the CONUS WELD July 2010 monthly products illustrated in Figs. 4 and 5 respectively. Data extracted by sampling regularly every 40 rows and 40 columns and discarding all cloudy and saturated 30 m WELD pixels. A total of 5,494,113 30 m pixels considered. Histogram X-axis bin widths of 0.015 NDVI.

5.2. Quantitative 12 month results

5.2.1. Data sample and out of range analysis results

The spatial sampling every 40 rows and 40 columns across the 501 CONUS WELD tiles and the cloud and saturation filtering provided more than 53 million 30 m pixels with TOA and corresponding surface reflectance values (Table 1). When only "good" quality 30 m atmospherically corrected pixels were considered, defined as those pixels computed using no natural neighbor interpolated MODIS 0.05° atmospheric correction coefficients, there were more than 19.6 million pixel sampled (Table 2). This amount of data was assumed to be sufficiently comprehensive to characterize 12 months of CONUS surface and atmospheric variations.

Tables 1 and 2 also summarize the percentage of pixels with out of range surface reflectance and surface NDVI considering all the data and only the "good" quality data respectively. The percentage of pixels with surface reflectance greater than the nominal theoretical upper limit (i.e., $\rho^s_\lambda > 1$) is negligible (less than 0.1%) for both the "good" quality and all the data. However, the percentage of pixels with surface reflectance less than the nominal theoretical lower limit (i.e., $\rho^s_\lambda < 0$) varies from about 0.4% (green reflectance) to about 1.5% (Landsat ETM+ band 7) when all the data are considered and is only negligible when considering the "good" quality data. These percentages although quite small may have considerable impact on applications that use the atmospherically corrected data. The percentage of pixels with surface NDVI outside nominal theoretical limits is about 0.3% ($NDVI^s < -1$) and 0.2% ($NDVI^s > 1$) when considering all the data but is negligible for the "good" quality data. The unusually high and low NDVI values occur over coastal and inland waters when the surface red and near infrared reflectance is close to zero. The difference between the results in Table 1 (all data) and Table 2 (good quality data) indicates the efficacy of the count the number of natural neighbor interpolated MODIS 0.05° atmospheric correction coefficients as a 30 m Landsat atmospheric correction quality indicator.

5.2.2. Sample scatterplot results

Fig. 8 shows scatter plots of the TOA and MODIS-corrected surface reflectance for all the reflective bands and also the NDVI extracted from the 12 months of CONUS WELD monthly products (more than 53 million pixel values, Table 1). The frequency of occurrence of the reflectance values per band is shown with a color scale for illustrative purposes. The majority of the pixels have reflectance associated with vegetation and soil surfaces and a relative minority have higher reflectance associated with sub-pixel and residual cloud contamination and also with snow and ice which were not removed from the analysis. The dotted lines show 1:1 lines superimposed for reference and the solid lines show reduced major axis (RMA) linear regression fits. For all the spectral bands the RMA regression intercepts are close to zero and the slopes (Table 3) are greater than unity because Rayleigh and aerosol backscatter into the sensor adds to the TOA signal at low surface reflectance ranges and aerosol absorption attenuates the TOA signal at higher surface reflectance (Ju et al., 2012; Kaufman & Sendra, 1988; Tanre et al., 1981). Similarly, the NDVI slope is 1.1 with a 0.03 intercept because, as discussed above with respect to Fig. 7, the atmosphere generally reduces NDVI. The surface NDVI for a relative minority of pixels is very different from the TOA NDVI (differences greater than 0.5) and this is examined in detail below.

Fig. 9 illustrates the mean and standard deviation of the difference between the surface and TOA reflectance (Eqs. (3) and (4)) defined over 100 contiguous surface reflectance ranging from 0 to 1, and also for the difference between the surface and TOA NDVI defined over 100 contiguous surface NDVI ranging from −1 to 1. The number of pixels in each illustrated range is shown (open circles) and varies from more than 16.8 million pixels (2^{24}), occurring at wavelengths corresponding predominantly to the reflectance of vegetated surfaces, to relatively fewer highly reflective pixel values associated with bright soils, snow, ice and sub-pixel and residual cloud. Table 4 summarizes the minimum and maximum mean and standard deviation differences over the 100 contiguous surface reflectance and surface NDVI ranges illustrated in Fig. 9.

The impact of the MODIS-based atmospheric correction is quite apparent in Fig. 9 and Table 4. The mean difference between the surface and TOA reflectance (Fig. 9, solid circles) increases monotonically with increasing surface reflectance, from negative differences at low surface reflectance changing to positive differences at higher reflectance. The change from a negative to a positive mean difference occurs when the surface reflectance is about 0.36, 0.22, 0.17, 0.14, 0.07, and 0.02 for reflective bands 1, 2, 3, 4, 5, and 7 respectively and illustrates the dependency between the surface reflectance and the atmospheric contribution to the TOA reflectance (Kaufman & Sendra, 1988; Tanre et al., 1981). Atmospheric impacts are greatest at the shorter Landsat ETM+ wavelengths. On average, the blue surface reflectance is about 0.08 smaller than the TOA reflectance at low blue surface reflectance and about 0.14 greater than the TOA reflectance at high blue surface reflectance. Landsat ETM+ band 5 reflects the least impact with surface reflectance on average about 0.002 smaller than the TOA reflectance at low band 5 surface reflectance and about 0.05 greater than the TOA reflectance at high band 5 surface reflectance. The standard deviation of the difference between the surface and TOA reflectance (vertical lines, Fig. 9) also increases generally monotonically with increasing surface reflectance.

The NDVI results summarized in Fig. 9 and Table 4 are more complicated than the red and near-infrared reflective wavelength results because of the non-linear NDVI red and near-infrared ratio formulation. On average the surface NDVI is about 0.1 greater than the TOA NDVI for much of the "vegetated" surface NDVI range from about 0.2 to about 0.8. The surface NDVI is greater than the TOA NDVI for "non-vegetated" surface NDVI in the range of about −0.1 to 0.1, which is also clearly apparent in the single month July histogram (Fig. 7). The

Table 1
The number of 30 m pixel values extracted every 40 rows and 40 columns from the 501 CONUS WELD tiles for each of 12 monthly products, discarding all cloudy and saturated pixels, and the percentage of pixels with MODIS-based atmospherically corrected surface reflectance and NDVI values outside nominal theoretical limits.

Landsat ETM+ reflective band or NDVI	Number of 30 m pixel values	Percentage (%) of pixels with surface reflectance or NDVI less than nominal theoretical lower limit (i.e. $\rho^s_\lambda < 0, NDVI^s < -1$)	Percentage (%) of pixels with surface reflectance or NDVI greater than nominal theoretical upper limit (i.e. $\rho^s_\lambda > 1, NDVI^s > 1$)
1	53,081,229	0.4761	0.0303
2	53,315,086	0.3680	0.0709
3	53,163,464	0.6726	0.0583
4	53,689,479	0.9271	0.0465
5	53,696,317	1.0619	0
7	53,713,611	1.4587	0
NDVI	53,158,943	0.2814	0.2074

Table 2
The same as Table 1 but considering only "good" quality 30 m atmospherically corrected pixels.

Landsat ETM+ reflective band or NDVI	Number of 30 m pixel values considered	Percentage (%) of pixels with surface reflectance or NDVI less than nominal theoretical lower limit (i.e. $\rho^s_\lambda < 0, NDVI^s < -1$)	Percentage (%) of pixels with surface reflectance or NDVI greater than nominal theoretical upper limit (i.e. $\rho^s_\lambda > 1, NDVI^s > 1$)
1	19,681,590	0.0336	0.0004
2	19,681,595	0.0015	0
3	19,680,851	0.0032	0
4	19,681,723	0.0007	0
5	19,679,934	0.0142	0
7	19,681,575	0.0611	0
NDVI	19,680,848	0.0004	0.0032

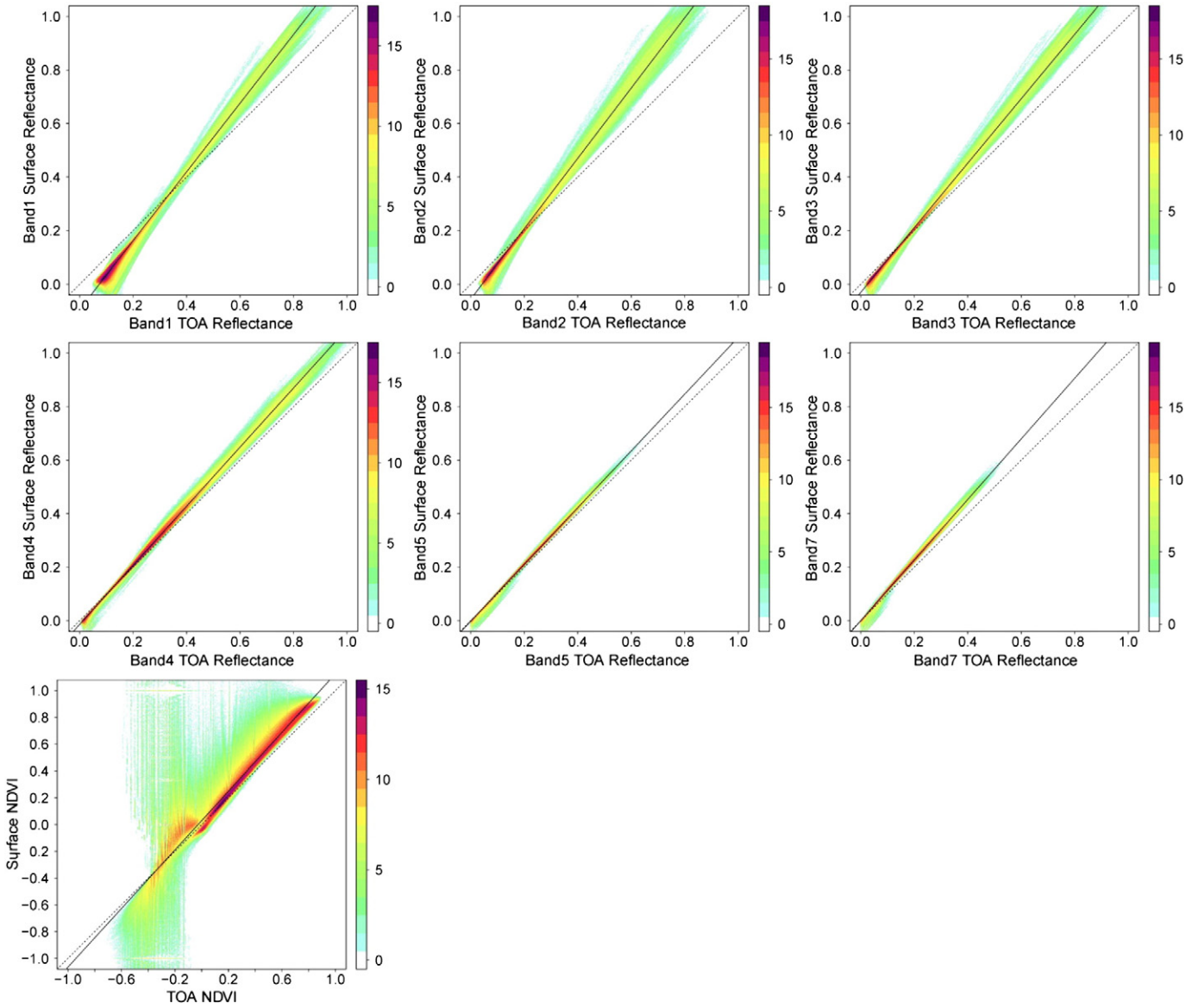

Fig. 8. Scatter plots of MODIS based atmospherically corrected WELD surface reflectance and derived NDVI (Y-axis) versus top of atmosphere (TOA) equivalents (X-axis). Data extracted by sampling regularly every 40 rows and 40 columns from across every WELD CONUS atmospherically corrected and TOA reflectance composite and discarding all cloudy and saturated WELD pixels. Data from all 12 monthly composites, December 2009 to November 2010, considered. A total of more than 53 million 30 m pixel values per band (Table 1). The solid lines show reduced major axis (RMA) orthogonal regression fits of these data. The dotted lines are 1:1 lines superimposed for reference. The frequency of occurrence of pixels with the same reflectance is illustrated by colors shaded with a $\log_2$ scale from 0 (white), 30 (green, $\log_2(5) = 2^5 = 32$), 1000 (orange, $2^{10} = 1024$), and >32,000 (purple, $2^{15} = 32{,}768$).

standard deviation of the differences is relatively high in the near zero NDVI range and reflects that water and other surfaces with near zero red and near-infrared reflectance provide unreliable NDVI (Verstraete & Pinty, 1996). Near-zero surface NDVI is particularly sensitive to any "over correction" by the atmospheric correction algorithm and any Landsat calibration errors. The greatest impact of the atmosphere on the NDVI occurs for surface NDVI close to the upper and lower NDVI theoretical limits. The mean difference between the surface and TOA NDVI is −0.63 when the surface NDVI is −1 and 0.57 when the surface NDVI is 1.0. However these unusually high and low NDVI values only occur over coastal waters when the surface red and near infrared reflectance are close to zero.

Table 3
Slopes and intercepts of the reduced major axis (RMA) linear regression fits of the MODIS-corrected surface reflectance and TOA reflectance data illustrated in Fig. 8 and the number of 30 m pixel values extracted by sampling regularly every 40 rows and 40 columns from all 12 monthly WELD products and discarding all cloudy and saturated WELD pixels.

Landsat ETM+ reflective band or NDVI	RMA slope	RMA intercept	Number of 30 m pixel values considered
1	1.2843	−0.0944	53,081,229
2	1.3134	−0.0557	53,315,086
3	1.2046	−0.0301	53,163,464
4	1.1050	−0.0142	53,689,479
5	1.0612	0.0023	53,696,317
7	1.1329	0.0001	53,713,611
NDVI	1.0956	0.0299	53,158,943

Fig. 10 shows the results as illustrated in Fig. 8 but derived considering only "good" quality 30 m atmospherically corrected pixels defined as pixels with surface reflectance computed using no natural neighbor interpolated MODIS 0.05° atmospheric correction coefficients. This reduced the more than 53 million non-cloud and unsaturated reflectance values per band for the 12 months (Table 1) to about 19.6 million "good" quality 30 m pixel values per band (Table 2). Despite this reduction in sample size, the RMA regression slopes are greater than one and

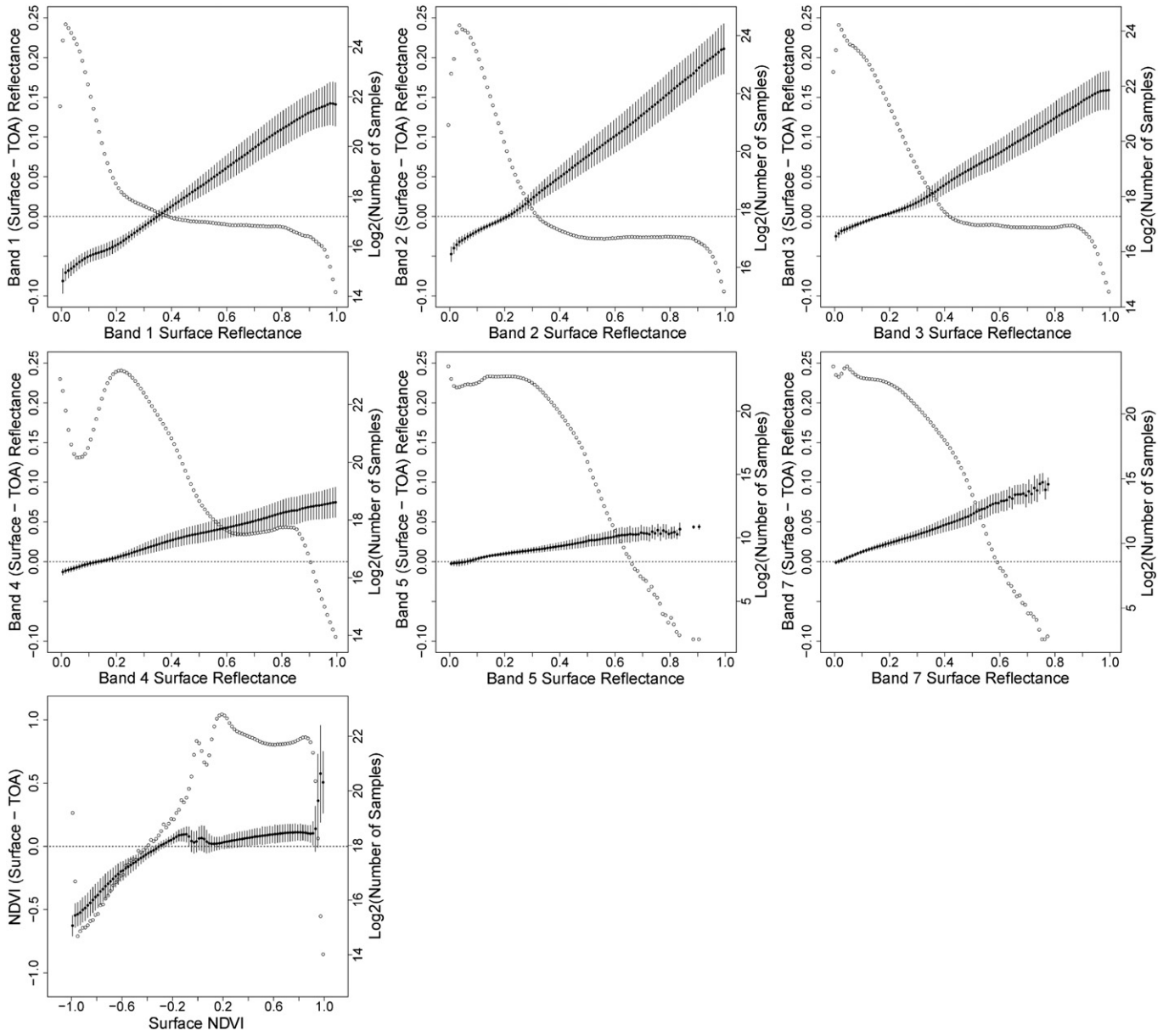

Fig. 9. Mean (solid circles) ± one standard deviation (error bars) of the spectral differences between MODIS based atmospherically corrected reflectance WELD surface and top of atmosphere (TOA) reflectance (left Y-axis) for contiguous 0.01 surface reflectance ranges (X-axis). The results for NDVI derived from the surface and TOA red and near-infrared reflectance are also shown. The number of 30 m pixel values considered (log_2 scale) is shown by the open circles (right Y-axis). Data the same as illustrated in Fig. 8, i.e., extracted by sampling regularly every 40 rows and 40 columns from across every WELD CONUS atmospherically corrected and TOA reflectance composite and discarding all cloudy and saturated WELD pixels. Data from all 12 monthly composites considered. A total of more than 53 million 30 m pixel values per band (Table 1).

Table 4

Summary of the range of the 100 mean $(\overline{\Delta}\rho_{\lambda,k})$ and standard deviation $\left(\sigma_{\Delta\rho_{\lambda,k}}\right)$ reflectance differences between the MODIS based atmospherically corrected WELD surface reflectance and top of atmosphere reflectance, and similarly derived NDVI, that are illustrated in Fig. 9.

Landsat ETM+ reflective band or NDVI	Minimum mean difference	Maximum mean difference	Minimum standard deviation difference	Maximum standard deviation difference
1	−0.081	0.142	0.0056	0.0272
2	−0.047	0.210	0.0031	0.0315
3	−0.025	0.159	0.002	0.0242
4	−0.013	0.075	0.0028	0.0188
5	−0.002	0.053	0.0017	0.0104
7	−0.001	0.127	0.0022	0.0159
NDVI	−0.629	0.573	0.0298	0.3838

the intercepts close to zero (Table 5) and are similar to those computed using all the data (Table 3). Comparing Figs. 8 and 10 it is apparent that considering only "good" quality pixels removed many pixels with high reflectance. This was because "good" quality pixels tend to be away from cloudy locations as clouds preclude the MODIS Terra atmospheric retrievals (Figs. 1 and 2) and are less likely to include residual and sub-pixel clouds that were not detected by the two 30 m WELD cloud masks.

Fig. 11 and Table 6 show the same results as illustrated in Fig. 9 and Table 4 but derived considering only the "good" quality 30 m atmospherically corrected pixels. The range of the mean and standard deviation reflectance and NDVI differences (Eqs. (3) and (4)) is consistently smaller for all ETM+ bands and for the NDVI when good quality pixels only are considered. This is expected as the atmospheric correction undertaken with spatially interpolated atmospheric correction coefficients

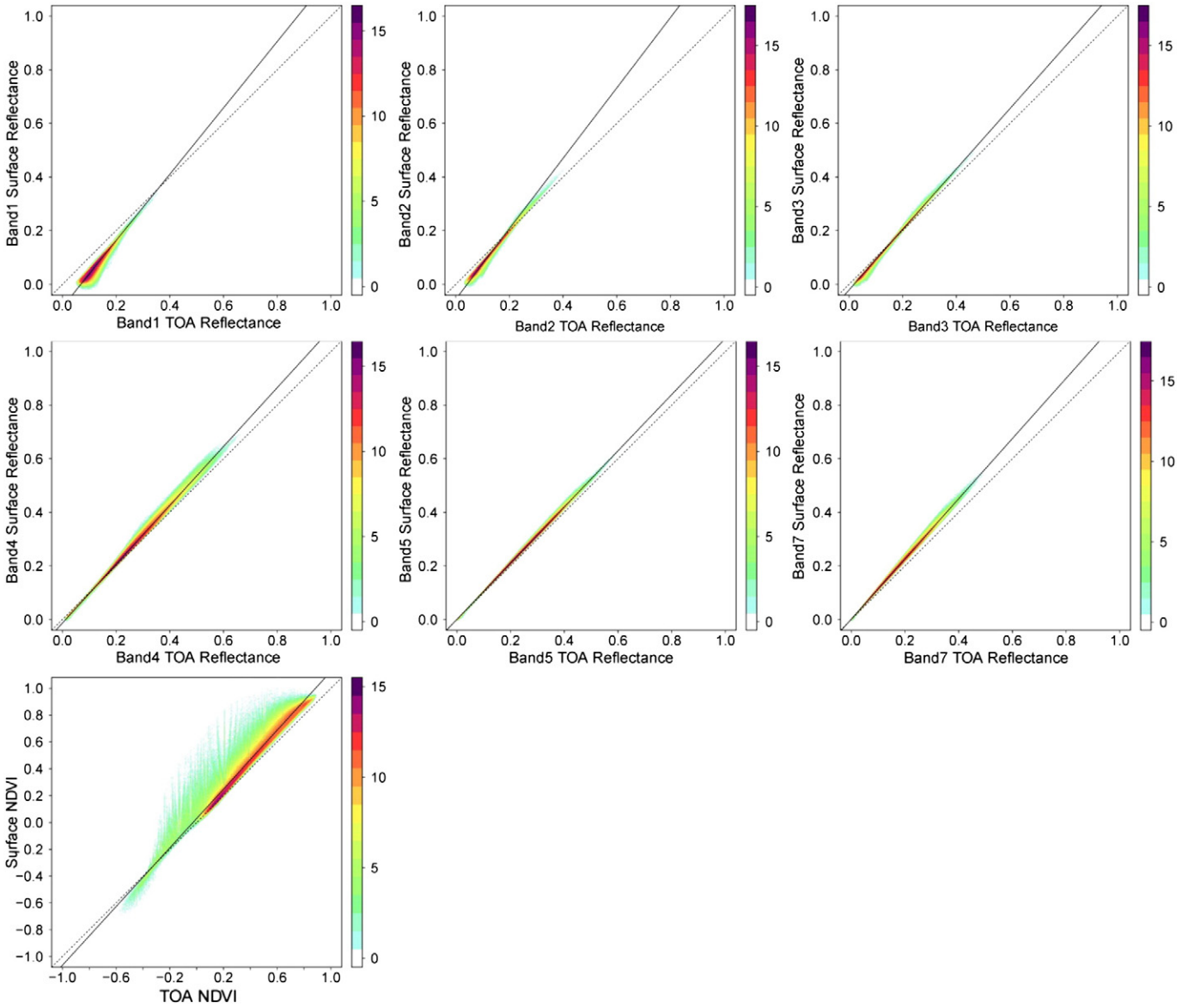

Fig. 10. The same as Fig. 8 but only considering "good" quality 30 m atmospherically corrected pixels computed using no natural neighbor interpolated MODIS 0.05° atmospheric correction coefficients. A total of more than 19.6 million 30 m pixel values per band (Table 2). The solid lines show reduced major axis (RMA) orthogonal regression fits of these data. The dotted lines are 1:1 lines superimposed for reference.

is less likely to be reliable and also because the good quality pixels are less likely to be close to clouds or to include residual and sub-pixel clouds that were undetected by the two 30 m WELD cloud masks.

Table 5
Slopes and intercepts of the reduced major axis (RMA) linear regression fits of the MODIS-corrected surface reflectance and TOA reflectance data illustrated in Fig. 10 (i.e., considering only "good" quality 30 m atmospherically corrected pixels) and the number of 30 m pixel values extracted by sampling regularly every 40 rows and 40 columns from all 12 monthly WELD products and discarding all cloudy and saturated WELD pixels.

Landsat ETM+ reflective band or NDVI	RMA slope	RMA intercept	Number of 30 m pixel values considered
1	1.2377	−0.0848	19,681,590
2	1.2052	−0.0423	19,681,595
3	1.1276	−0.0210	19,680,851
4	1.0983	−0.0135	19,681,723
5	1.0487	0.0002	19,679,934
7	1.1231	0.0013	19,681,575
NDVI	1.1322	0.0049	19,680,848

5.2.3. Sample TOA to surface mean and relative absolute difference results

Table 7 summarizes the mean magnitude of the difference between the surface and TOA reflectance and NDVI. The mean absolute difference between the surface and TOA reflectance ($|\overline{\Delta}|\rho_\lambda$, Eq. (5)) and the mean reflectance normalized absolute percentage difference ($|\overline{\Delta}|^*\rho_\lambda$, Eq. (6)) are shown for each reflective wavelength band and for the NDVI. The $|\overline{\Delta}|\rho_\lambda$ values reflect the absolute magnitude of the differences illustrated in Figs. 9 and 11 and show greater differences at shorter Landsat wavelength bands, with the exception of Landsat band 7. This spectral pattern was observed in the CONUS MODIS-based validation results reported in Ju et al. (2012). The mean reflectance normalized absolute percentage differences $\left(|\overline{\Delta}|^*\rho_\lambda\right)$ enable more meaningful comparison among bands. Considering all 53 million CONUS pixels the $|\overline{\Delta}|^*\rho_\lambda$ values are 45%, 22%, 12%, 6%, 5%, and 13% for Landsat ETM+ bands 1, 2, 3, 4, 5, 7 respectively and 28% for the NDVI. When only "good" quality pixels are considered the $|\overline{\Delta}|^*\rho_\lambda$ values are reduced compared to considering all the data, with the exception of the blue band. The $|\overline{\Delta}|^*\rho_\lambda$ values considering the good quality data are 51%, 19%, 8%, 4%, 5%, and 13% for Landsat

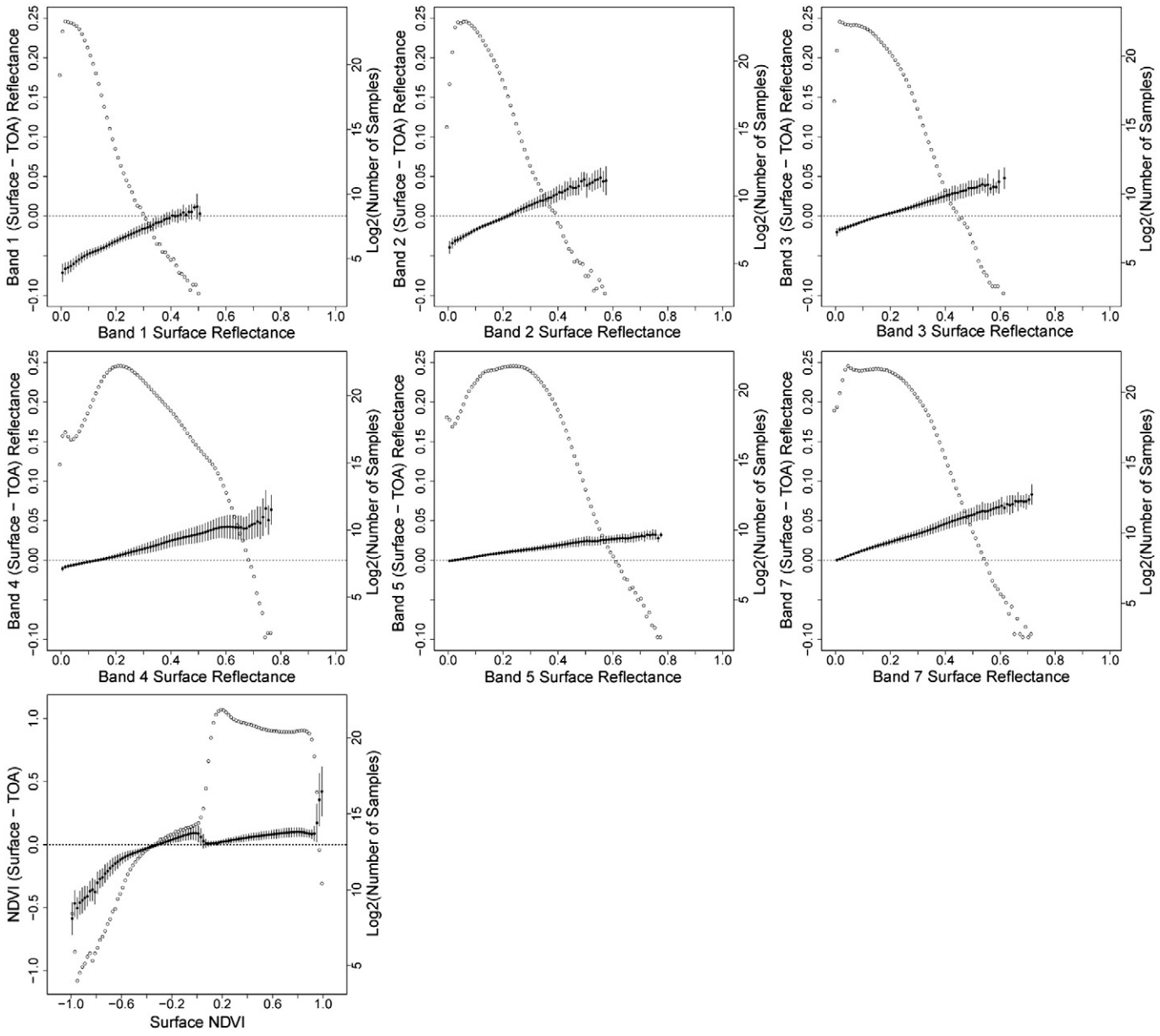

Fig. 11. As Fig. 9 but only using the data illustrated in Fig. 10 that consider only "good" quality 30 m atmospherically corrected pixels computed using no natural neighbor interpolated MODIS 0.05° atmospheric correction coefficients. A total of more than 19.6 million 30 m pixel values per band (Table 2).

Table 6

Summary of the range of the 100 mean $(\overline{\Delta}\rho_{\lambda,k})$ and standard deviation $\left(\sigma_{\Delta\rho_{\lambda,k}}\right)$ reflectance differences between the MODIS based atmospherically corrected WELD surface reflectance and top of atmosphere reflectance, and similarly derived NDVI, that are illustrated in Fig. 11 (i.e., considering only "good" quality 30 m atmospherically corrected pixels).

Landsat ETM+ reflective band or NDVI	Minimum mean difference	Maximum mean difference	Minimum standard deviation difference	Maximum standard deviation difference
1	−0.072	0.012	0.004	0.015
2	−0.040	0.046	0.002	0.015
3	−0.020	0.036	0.002	0.010
4	−0.010	0.034	0.002	0.011
5	−0.001	0.024	0.001	0.006
7	0.000	0.058	0.001	0.009
NDVI	−0.587	0.092	0.014	0.129

Table 7

The mean absolute difference between the surface and TOA reflectance $|\overline{\Delta}|\rho_\lambda$ and the mean reflectance normalized absolute percentage difference $|\overline{\Delta}|^*\rho_\lambda$ derived from 12 months of CONUS cloud-free and unsaturated pixels, a total of more than 53 million 30 m pixel values per band (Table 1) and considering only "good" quality 30 m atmospherically corrected pixels, a total of more than 19.6 million 30 m pixel values per band (Table 2).

Landsat ETM+ reflective band or NDVI	$\lvert\overline{\Delta}\rvert\rho_\lambda$	$\lvert\overline{\Delta}\rvert\rho_\lambda$ derived considering only "good" quality 30 m atmospherically corrected pixels.	$\lvert\overline{\Delta}\rvert^*\rho_\lambda$	$\lvert\overline{\Delta}\rvert^*\rho_\lambda$ derived considering only "good" quality 30 m atmospherically corrected pixels
1	0.061	0.058	45.5%	50.8%
2	0.027	0.020	21.9%	18.7%
3	0.015	0.008	12.3%	7.7%
4	0.013	0.010	5.7%	4.2%
5	0.009	0.011	5.3%	5.0%
7	0.015	0.018	13.4%	13.2%
NDVI	0.084	0.054	28.1%	14.6%

ETM + bands 1, 2, 3, 4, 5, 7 respectively and 15% for the NDVI. Thus on average for the 12 months of CONUS data considered the surface NDVI is 28% different from the TOA NDVI when all the data are considered and is 15% different when only the good quality atmospherically corrected data are considered.

5.3. Temporal land cover based results

Figs. 12 and 13 show time series plots of the monthly mean and standard deviation of the TOA (filled circles) and surface (open circles) red and near-infrared reflectance and derived NDVI for the CONUS bare ground and forest pixels (Fig. 3) respectively. The top and bottom rows illustrate the summary statistics computed considering all and only the good quality cloud-free unsaturated data respectively.

The bare ground results (Fig. 12) were computed using more than 1 million to more than 1.9 million 30 m bare ground pixel values per month (top row) and more than 430,000 to more than 990,000 pixel values per month when only "good" quality pixels were considered (bottom row). The monthly mean surface red and near-infrared surface reflectance values are higher than the TOA equivalents. This was observed in Figs. 8 and 10 for the majority of the CONUS sampled pixels with red and near-infrared reflectance similar to the mean soil values illustrated in Fig. 12. The winter red and near-infrared reflectance values have higher means and standard deviations than in other months when all the data are considered (top row) which is associated primarily with snow over the northern CONUS states. When only good quality data are considered the snow effects are less apparent (bottom row) because the majority of the northern CONUS states have above average Winter cloud cover at the time of Landsat overpass (Ju & Roy, 2008) and so there are relatively fewer snowy locations encompassed by the good quality pixels. The monthly mean surface NDVI values are consistently higher than the TOA NDVI. Considering the good quality data, the minimum, mean and maximum monthly NDVI difference between the TOA and surface mean NDVI is 0.005, 0.010, and 0.014 respectively. These differences are quite small because of low NDVI of bare soil and impermeable urban surfaces (mean of the 12 monthly mean TOA and surface NDVI is 0.131 and 0.142 respectively) which have little temporal variation.

The forest results (Fig. 13) were computed using more than 2.4 million to more than 4.6 million 30 m bare ground pixel values per month (top row) and more than 750,000 to nearly 2.1 million pixel values per month when only "good" quality pixels were considered (bottom row). The monthly mean surface red and near-infrared reflectance values are lower and higher than the TOA equivalents respectively due to the spectral dependence of the atmospheric scattering and absorption (evident in Figs. 8 to 11). The standard deviation of the monthly red and near-infrared reflectance and NDVI are quite high reflecting the wide variation in forest types sampled across the CONUS (Fig. 3). Despite this diversity, a CONUS forest phenology is evident similar to that of a temperate deciduous broad-leaf forest with high NDVI (~0.8) in May–September and rapid phenological change in the spring (March–April) and autumn (October–November) (Fisher & Mustard, 2007; Schwartz, Reed, & White, 2002). As with the bare ground results, the red and near-infrared reflectance monthly mean and standard deviation values are greater in the winter months. This is associated with snow, as although evergreen forests may hide snow, deciduous forests shed their leaves in the winter months to expose underlying soil (Betts, 2000). Snow increases least the reflectance of vegetated surfaces with high canopy density and vertical structure (e.g., evergreen forests) and increases most the reflectance of surfaces with sparse and/or short vegetation (e.g., bare ground) (Barnes & Roy, 2010; Gao et al., 2005). The monthly mean surface NDVI values are consistently higher than the TOA NDVI. Considering the good quality data the mean monthly surface NDVI is higher than the mean monthly TOA NDVI by 0.100 and the minimum and maximum monthly NDVI differences are 0.073 and 0.134 respectively.

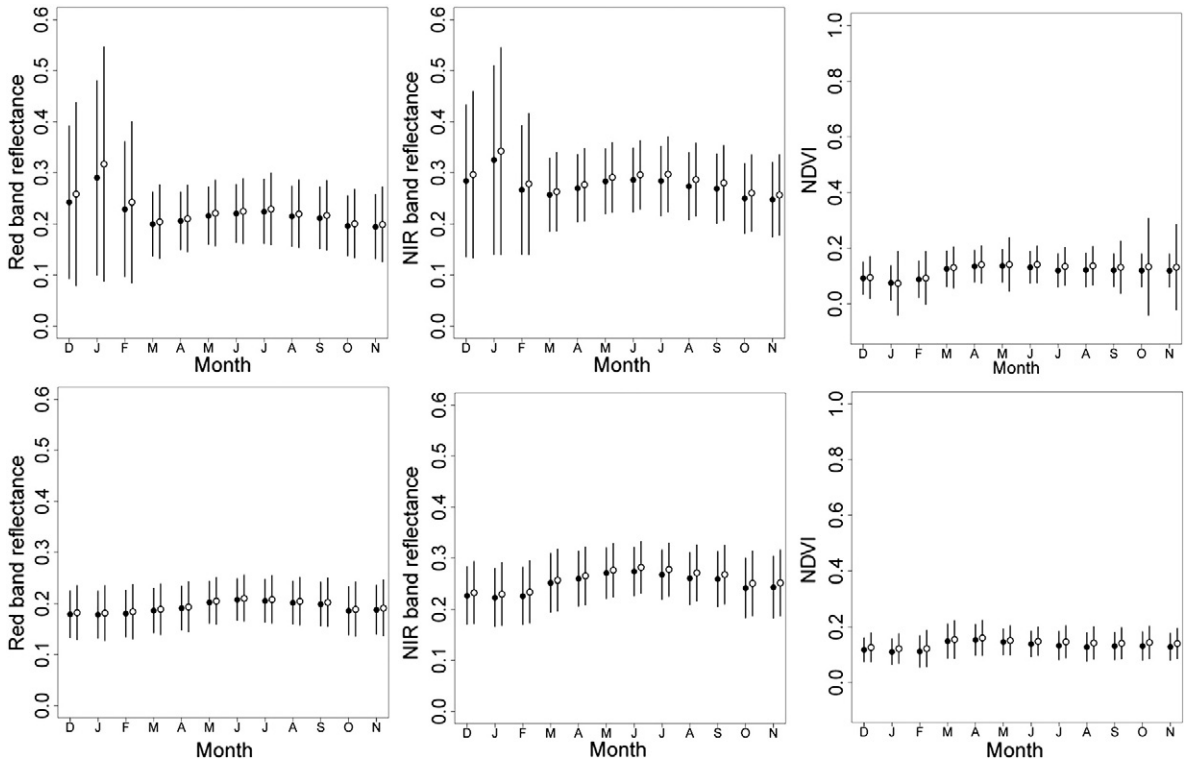

Fig. 12. Summary CONUS statistics (mean ± standard deviation) of top of atmosphere (filled circles) and MODIS based atmospherically corrected (open circles) red and near-infrared WELD reflectance and derived NDVI for Bare Ground pixels (orange, Fig. 3). Extracted from the 12 monthly (December 2009 to November 2010) WELD monthly products considering only non-cloudy non-saturated WELD values at the locations of 30 m bare ground pixels. The bottom row shows the results considering only "good" quality 30 m atmospherically corrected pixels computed using no natural neighbor interpolated MODIS 0.05° atmospheric correction coefficients.

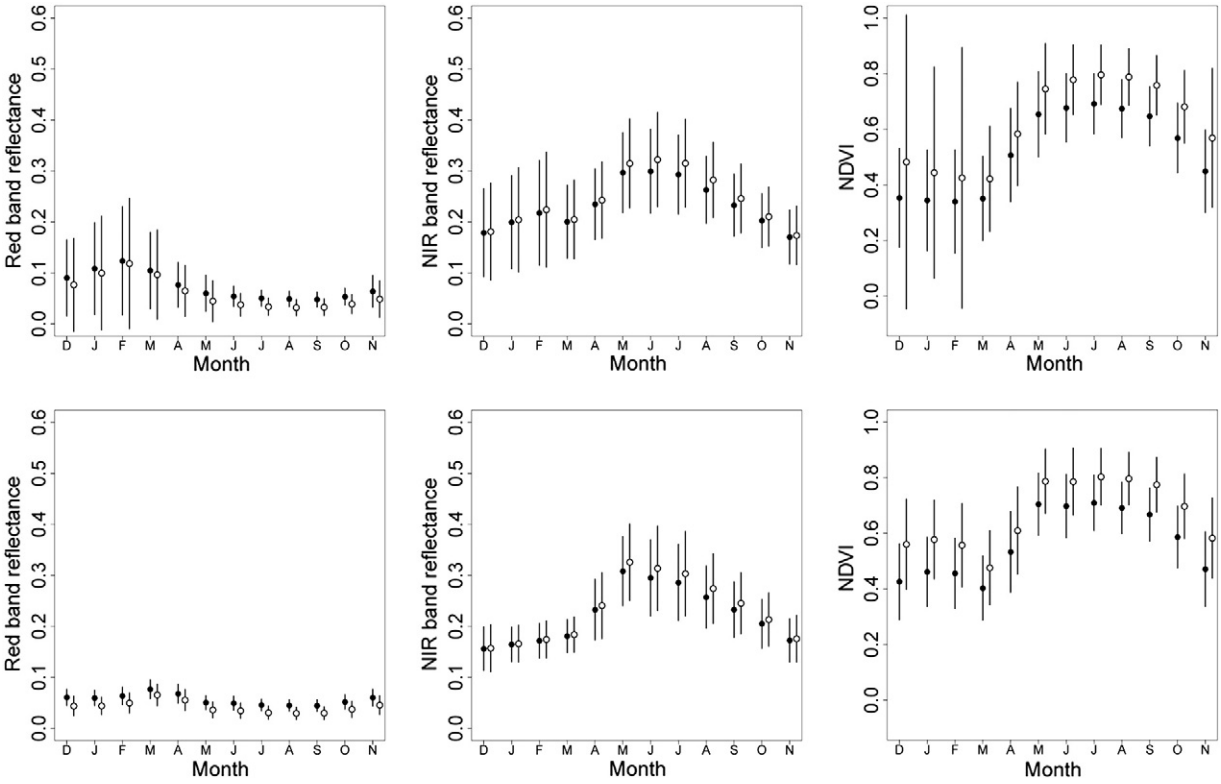

Fig. 13. Summary CONUS statistics (mean ± standard deviation) of top of atmosphere (filled circles) and MODIS based atmospherically corrected (open circles) red and near-infrared WELD reflectance and derived NDVI for forest pixels (green, Fig. 3). Extracted from the 12 monthly (December 2009 to November 2010) WELD monthly products considering only non-cloudy non-saturated WELD values at the locations of 30 m forest pixels. The bottom row shows the results considering only "good" quality 30 m atmospherically corrected pixels computed using no natural neighbor interpolated MODIS 0.05° atmospheric correction coefficients.

6. Conclusion

The integration of a recent MODIS based Landsat atmospheric correction algorithm (Ju et al., 2012) into the Web-enabled Landsat Data (WELD) processing (Roy et al., 2010) was described and demonstrated by application to 12 months of conterminous United States (CONUS) Landsat 7 ETM+ data (8116 ETM+ acquisitions). The algorithm uses 0.05° atmospheric characterization data retrieved from MODIS Terra to atmospherically correct contemporaneous (same orbit) Landsat 7 ETM+ reflectance using the 6SV radiative transfer code. The differences between top of atmosphere (TOA) and surface Landsat 7 ETM+ reflectance and derived NDVI were quantified with respect to spectral, temporal, land cover, and a per-pixel atmospheric correction quality storage scheme. A sample of 53 million pixels extracted across the CONUS and from 12 months of data was considered to capture surface and atmospheric variability. The major findings of this study are:

- The mean absolute differences between surface and TOA reflectance expressed as percentages of the surface reflectance were 45%, 22%, 12%, 6%, 5%, and 13% for Landsat ETM+ bands 1 (0.45–0.52 μm), 2 (0.53–0.61 μm), 3 (0.63–0.69 μm), 4 (0.78–0.90 μm), 5 (1.55–1.75 μm) and 7 (2.09–2.35 μm) respectively. This quantifies the average CONUS Landsat ETM+ spectral dependency of atmospheric scattering and absorption that is particularly large for the shorter wavelength ETM+ bands.
- The mean difference between surface and TOA reflectance (surface minus TOA) increased monotonically with increasing surface reflectance. On average the change from a negative to a positive mean difference occurred when the surface reflectance was 0.36, 0.22, 0.17, 0.14, 0.07, and 0.02 for Landsat ETM+ reflective bands 1, 2, 3, 4, 5, and 7 respectively. This illustrates the established dependency between the surface reflectance and the atmospheric contribution to the TOA reflectance (Kaufman & Sendra, 1988; Tanre et al., 1981). These values are of interest as they depict the average CONUS Landsat ETM+ surface reflectance values where the atmosphere has on average no impact and provide the average boundary values for positive and negative atmospheric contributions to ETM+ TOA reflectance.
- The mean absolute difference between surface and TOA NDVI expressed as a percentage of the surface NDVI was 28%. The surface NDVI was on average 0.1 greater than the TOA NDVI for the "vegetated" surface NDVI range from about 0.2 to about 0.8. These average CONUS differences are quite large and illustrate the broad utility of maximum NDVI compositing to select pixels with reduced atmospheric effects from satellite time series (Holben, 1986).
- The spectral dependence of atmospheric scattering and absorption was observed in CONUS monthly forest and bare ground red, near-infrared and NDVI time series. The mean monthly surface near-infrared reflectance and NDVI were higher than the TOA equivalents for the CONUS forest and bare ground pixels, and the mean monthly surface red reflectance was lower and higher than the TOA red reflectance for the forest and bare ground pixels respectively.
- The atmospheric correction quality storage scheme broadly characterized the quality of the atmospherically data. Good quality 30 m atmospherically corrected pixels were defined as those pixels computed using no interpolated MODIS 0.05° atmospheric correction coefficients. The range of the mean and standard deviation reflectance and NDVI differences between TOA and surface CONUS values was smaller for all Landsat ETM+ bands and for the NDVI when good quality pixels only were considered. This is expected as atmospheric correction undertaken with spatially interpolated atmospheric characterization data is less likely to be

reliable and because good quality pixels are less likely to be close to clouds or to include residual and sub-pixel clouds that may deleteriously impact the atmospheric correction (Kaufman, 1987; Ouaidrari & Vermote, 1999; Tackett & Di Girolamo, 2009).

With the advent of the free U.S. Landsat data policy (Wulder, Masek, Cohen, Loveland, & Woodcock, 2012) it is now feasible to consider the generation of global coverage Landsat data sets (Gutman et al., 2008; Townshend et al., 2012; Tucker, Grant, & Dykstra, 2004) but generated using all the available Landsat data, for example, global monthly WELD Landsat data sets composed of data sensed by different sensors such as Landsat 5 Thematic Mapper (TM) and Landsat 7 ETM+ (Kovalskyy & Roy, 2013). Multiple Landsat sensor data could be fused by compositing and then the atmospheric correction undertaken in the manner described in this paper. Further research is needed however to assess the applicability of the MODIS-based atmospheric correction algorithm to Landsat 5 TM data as although the Landsat 5 and 7 satellites are in the same orbit they have different overpass times. The MODIS-based atmospheric correction algorithm assumes that the atmosphere at the time of MODIS Terra overpass is sufficiently representative of the atmospheric conditions at the approximately 25 minute earlier Landsat 7 ETM+ overpass time (Ju et al., 2012). This is a reasonable assumption, except for rapidly moving atmospheres and for dynamic aerosol events (e.g., due to biomass burning and dust storms), but will be less valid for Landsat 5 which overpasses about 40 minutes earlier than MODIS Terra. Finally, we note that the MODIS-based atmospheric correction method is not applicable to pre-2000 Landsat data when MODIS Terra was not in orbit and is not applicable to MODIS Aqua data, available since 2002, because the Aqua satellite is in an afternoon constellation with a different orbit to the morning constellation Landsat 5 and 7 and MODIS Terra orbits (Demarest, Good, & Rand, 2001).

Acknowledgements

This research was funded by NASA grant number NNX08AL93A. The U.S. Landsat project management and staff at USGS EROS, Sioux Falls, South Dakota are thanked for provision of the Landsat ETM+ data. The anonymous reviewers are thanked for their comments that improved this paper.

References

Barnes, C. A., & Roy, D. P. (2010). Radiative forcing over the conterminous United States due to contemporary land cover land use change and sensitivity to snow and interannual albedo variability. *Journal of Geophysical Research*, *115*, G04033. http://dx.doi.org/10.1029/2010JG001428.

Betts, R. A. (2000). Offset of the potential carbon sink from boreal forestation by decreases in surface albedo. *Nature*, *408*, 187–190.

Bindschadler, R., Vornberger, P., Fleming, A., Fox, A., Mullins, J., Binnie, D., et al. (2008). The Landsat image mosaic of Antarctica. *Remote Sensing of Environment*, *112*, 4214–4226.

Cahalan, R. F., Oreopoulos, L., Wen, G. Y., Marshak, A., Tsay, S.C., & DeFelice, T. (2001). Cloud characterization and clear-sky correction from Landsat-7. *Remote Sensing of Environment*, *78*, 83–98.

Cihlar, J., Manak, D., & D' Iorio, M. (1994). Evaluation of compositing algorithms for AVHRR data over land. *IEEE Transactions on Geoscience and Remote Sensing*, *32*, 427–437.

Cohen, W. B., Maiersperger, T. K., Gower, S. T., & Turner, D. P. (2003). An improved strategy for regression of biophysical variables and Landsat ETM+ data. *Remote Sensing of Environment*, *84*, 561–571.

Demarest, P., Good, S., & Rand, D. (2001). Ascent plan for Aqua (EOS-PM1) including phasing with Terra (EOS-AM1). *Proceedings of 16th International Symposium on Space Flight Dynamics, Pasadena*.

Dowdeswell, J. A., & Mcintyre, N. F. (1986). The saturation of Landsat MSS detectors over large ice masses. *International Journal of Remote Sensing*, *7*, 151–164.

Dubovik, O., Holben, B., Eck, T. F., Smirnov, A., Kaufman, Y. J., King, M.D., et al. (2002). Variability of absorption and optical properties of key aerosol types observed in worldwide locations. *Journal of Atmospheric Sciences*, *59*, 590–608.

Fisher, J. I., & Mustard, J. F. (2007). Cross-scalar satellite phenology from ground Landsat and MODIS data. *Remote Sensing of Environment*, *109*, 261–273.

Gao, F., Schaaf, C. B., Strahler, A. H., Roesch, A., Lucht, W., & Dickinson, R. (2005). MODIS bidirectional reflectance distribution function and albedo Climate Modeling Grid products and the variability of albedo for major global vegetation types. *Journal of Geophysical Research*, *110*, D01104. http://dx.doi.org/10.1029/2004JD005190.

Gutman, G., Byrnes, R., Masek, J., Covington, S., Justice, C., Franks, S., et al. (2008). Towards monitoring land-cover and land-use changes at a global scale: The global land survey. *Photogrammetric Engineering and Remote Sensing*, *74*, 6–10.

Hansen, M. C., Egorov, A., Potapov, P. V., Stehman, S. V., Tyukavina, A., Turubanova, S. A., et al. (2013). Monitoring conterminous United States (CONUS) land cover change with Web-Enabled Landsat Data (WELD). *Remote Sensing of Environment*, *140*, 466–484.

Hansen, M. C., Egorov, A., Roy, D. P., Potapov, P., Ju, J., Turubanova, S., et al. (2011). Continuous fields of land cover for the conterminous United States using Landsat data: First results from the Web-Enabled Landsat Data (WELD) project. *Remote Sensing Letters*, *2*, 279–288.

Hansen, M. C., Stehman, S. V., & Potapov, P. V. (2010). Quantification of global gross forest cover loss. *Proceedings of the National Academy of Sciences*, *107*, 8650–8655.

Holben, B. (1986). Characteristics of maximum-value composite images from temporal AVHRR data. *International Journal of Remote Sensing*, *7*, 1417–1434.

Holben, B. N., Eck, T. F., Slutsker, I., Tanré, D., Buis, J. P., Setzer, A., et al. (1998). AERONET — A federated instrument network and data archive for aerosol characterization. *Remote Sensing of the Environment*, *66*, 1–16.

Homer, C., Huang, C., Yang, L., Wylie, B., & Coan, M. (2004). Development of a 2001 national landcover database for the United States. *Photogrammetric Engineering and Remote Sensing*, *70*, 829–840.

Huete, A. (1988). A soil-adjusted vegetation index (SAVI). *Remote Sensing of Environment*, *25*, 295–309.

Irish, R. I., Barker, J. L., Goward, S. N., & Arvidson, T. (2006). Characterization of the Landsat-7 ETM+ automated cloud-cover assessment (ACCA) algorithm. *Photogrammetric Engineering and Remote Sensing*, *72*, 1179–1188.

Ju, J., & Roy, D. P. (2008). The availability of cloud-free Landsat ETM+ data over the conterminous United States and globally. *Remote Sensing of Environment*, *112*, 1196–1211.

Ju, J., Roy, D. P., Vermote, E., Masek, J., & Kovalskyy, V. (2012). Continental-scale validation of MODIS-based and LEDAPS Landsat ETM+ atmospheric correction methods. *Remote Sensing of Environment*, *122*, 175–184.

Justice, C., Townshend, J., Vermote, E., Masuoka, E., Wolfe, R., Saleous, N., et al. (2002). An overview of MODIS Land data processing and product status. *Remote Sensing of Environment*, *83*, 3–15.

Kaufman, Y. J. (1987). The effect of subpixel clouds on remote sensing. *International Journal of Remote Sensing*, *8*, 839–857.

Kaufman, Y. J. (1989). The atmospheric effect on remote sensing and its correction. In G. Asrar (Ed.), *Theory and application of optical remote sensing* (pp. 341). New York: John Wiley & Sons.

Kaufman, Y. J., & Sendra, C. (1988). Algorithm for automatic corrections to visible and near IR satellite imagery. *International Journal of Remote Sensing*, *9*, 1357–1381.

Kaufman, Y. J., & Tanre, D. (1992). Atmospherically resistant vegetation index (ARVI) for EOS-MODIS. *IEEE Transactions on Geoscience and Remote Sensing*, *30*, 261–270.

Kaufman, Y. J., Tanre, D., Remer, L. A., Vermote, E. F., Chu, A., & Holben, B. N. (1997). Operational remote sensing of tropospheric aerosol over the land from EOS-MODIS. *Journal of Geophysical Research — Atmospheres*, *102*(14), 17051–17068.

Kotchenova, S., Vermote, E. R., Matarrese, R., & Klemm, F., Jr. (2006). Validation of a vector version of the 6S radiative transfer code for atmospheric correction of satellite data. Part I: Path radiance. *Applied Optics*, *45*, 6762–6774.

Kovalskyy, V., & Roy, D. P. (2013). The global availability of Landsat 5 TM and Landsat 7 ETM+ land surface observations and implications for global 30 m Landsat data product generation. *Remote Sensing of Environment*, *130*, 280–293.

Kovalskyy, V., Roy, D. P., Zhang, X., & Ju, J. (2011). The suitability of multi-temporal Web-Enabled Landsat Data (WELD) NDVI for phenological monitoring — A comparison with flux tower and MODIS NDVI. *Remote Sensing Letters*, *3*(4), 325–334.

Lee, D. S., Storey, J. C., Choate, M. J., & Hayes, R. (2004). Four years of Landsat-7 on-orbit geometric calibration and performance. *IEEE Transactions on Geoscience and Remote Sensing*, *42*, 2786–2795.

Liu, H. Q., & Huete, A.R. (1995). A feedback based modification of the NDVI to minimize canopy background and atmospheric noise. *IEEE Transactions on Geoscience and Remote Sensing*, *33*, 457–465.

Markham, B.L., & Helder, D. L. (2012). Forty-year calibrated record of earth-reflected radiance from Landsat: A review. *Remote Sensing of Environment*, *122*, 30–40.

Markham, B.L., Storey, J. C., Williams, D. L., & Irons, J. R. (2004). Landsat sensor performance: History and current status. *IEEE Transactions on Geoscience and Remote Sensing*, *42*, 2691–2694.

Masek, J. G., Vermote, E. F., Saleous, N. E., Wolfe, R., Hall, F. G., Huemmrich, K. F., et al. (2006). A Landsat surface reflectance dataset for North America, 1990–2000. *IEEE Transactions on Geoscience and Remote Sensing Letters*, *3*(1), 68–72.

McDonald, A. J., Gemmell, F. M., & Lewis, P. E. (1998). Investigation of the utility of spectral vegetation indices for determining information on coniferous forests. *Remote Sensing of Environment*, *66*(3), 250–272.

Miura, T., Huete, A.R., Yoshioka, H., & Holben, B. N. (2001). An error and sensitivity analysis of atmospheric resistant vegetation indices derived from dark target-based atmospheric correction. *Remote Sensing of Environment*, *78*, 284–298.

Ouaidrari, H., & Vermote, E. F. (1999). Operational atmospheric correction of Landsat TM data. *Remote Sensing of Environment*, *70*, 4–15.

Roy, D. P. (1997). Investigation of the maximum normalised difference vegetation index (NDVI) and the maximum surface temperature (Ts) AVHRR compositing procedures for the extraction of NDVI and Ts over forest. *International Journal of Remote Sensing*, *18*, 2383–2401.

Roy, D. P. (2000). The impact of misregistration upon composited wide field of view satellite data and implications for change detection. *IEEE Transactions on Geoscience and Remote Sensing*, *38*, 2017–2032.

Roy, D. P., Borak, J., Devadiga, S., Wolfe, R., Zheng, M., & Descloitres, J. (2002). The MODIS land product quality assessment approach. *Remote Sensing of Environment*, *83*, 62–76.

Roy, D. P., Ju, J., Kline, K., Scaramuzza, P. L., Kovalskyy, V., Hansen, M. C., et al. (2010). Web-enabled Landsat Data (WELD): Landsat ETM + composited mosaics of the conterminous United States. *Remote Sensing of Environment*, *114*, 35–49.

Roy, D. P., Ju, J., Kommareddy, I., Hansen, M., Vermote, E., & Zhang, C. (2011). Web-enabled Landsat data (Weld) products — Algorithm theoretical basis document. Available at: http://globalmonitoring.sdstate.edu/projects/weld/WELD_ATBD.pdf (last accessed September 1st 2013)

Roy, D. P., Lewis, P., Schaaf, C., Devadiga, S., & Boschetti, L. (2006). The Global impact of cloud on the production of MODIS bi-directional reflectance model based composites for terrestrial monitoring. *IEEE Geoscience and Remote Sensing Letters*, *3*, 452–456.

Schaepman-Strub, G., Schaepman, M. E., Painter, T. H., Dangel, S., & Martonchik, J. V. (2006). Reflectance quantities in optical remote sensing—Definitions and case studies. *Remote Sensing of Environment*, *103*, 27–42.

Schwartz, M.D., Reed, B. C., & White, M.A. (2002). Assessing satellite-derived start-of-season (SOS) measures in the conterminous USA. *International Journal of Climatology*, *22*, 1793–1805.

Sibson, R. (1981). A brief description of natural neighbor interpolation (chapter 2). In V. Barnett (Ed.), *Interpreting multivariate data* (pp. 21–36). Chichester: John Wiley.

Tackett, J. L., & Di Girolamo, L. (2009). Enhanced aerosol backscatter adjacent to tropical trade wind clouds revealed by satellite-based lidar. *Geophysical Research Letters*, *36*, L14804. http://dx.doi.org/10.1029/2009GL039264.

Tanre, D., Herman, M., & Deschamps, P. Y. (1981). Influence of the background contribution upon space measurements of ground reflectance. *Applied Optics*, *20*, 3676–3684.

Townshend, J. R., Masek, J. G., Huang, C., Vermote, E. F., Gao, F., Channan, S., et al. (2012). Global characterization and monitoring of forest cover using Landsat data: Opportunities and challenges. *International Journal of Digital Earth*. http://dx.doi.org/10.1080/17538947.2012.713190.

Tucker, C. J. (1979). Red and photographic infrared linear combinations for monitoring vegetation. *Remote Sensing of Environment*, *8*, 127–150.

Tucker, C. J., Grant, D.M., & Dykstra, J.D. (2004). NASA's global orthorectified Landsat data set. *Photogrammetric Engineering and Remote Sensing*, *70*, 313–322.

Vermote, E. F., El Saleous, N. Z., & Justice, C. O. (2002). Atmospheric correction of MODIS data in the visible to middle infrared: First results. *Remote Sensing of Environment*, *83*, 97–111.

Vermote, E. F., & Kotchenova, S. (2008). Atmospheric correction for the monitoring of land surfaces. *Journal of Geophysical Research*, *113*, D23S90. http://dx.doi.org/10.1029/2007JD009662.

Vermote, E. F., & Saleous, N. Z. (2006). In J. J. Qu, W. Gao, M. Kafatos, R. E. Murphy, & V. V. Salomonson (Eds.), *Operational atmospheric correction of MODIS visible to middle infrared land surface data in the case of an infinite Lambertian target. Earth science satellite remote sensing, science and instruments*, *Vol. 1*. (pp. 123–153). Springer (ch. 8).

Verstraete, M. M., & Pinty, B. (1996). Designing optimal spectral indexes for remote sensing applications. *IEEE Transactions on Geoscience and Remote Sensing*, *34*, 1254–1265.

Wolfe, R., Roy, D., & Vermote, E. (1998). The MODIS land data storage, gridding and compositing methodology: L2 grid. *IEEE Transactions on Geoscience and Remote Sensing*, *36*, 1324–1338.

Wulder, M.A., Masek, J. G., Cohen, W. B., Loveland, T. R., & Woodcock, C. E. (2012). Opening the archive: How free data has enabled the science and monitoring promise of Landsat. *Remote Sensing of Environment*, *122*, 2–10.

WWW1. http://globalmonitoring.sdstate.edu/projects/weld/ (WELD Version 1.5 Product Information Web Site, last accessed September 1st 2013)

WWW2. http://weld.cr.usgs.gov/ (WELD Version 1.5 Product Distribution Web Site, last accessed September 1st 2013)

WWW3. ftp://weldftp.cr.usgs.gov/CONUS_5Y_LandCover/ (WELD Version 1.5 CONUS Land Cover Land Cover Change (LCLCC) product Distribution FTP Site, last accessed September 1st 2013)